OBSERVATIONAL STUDIES OF ACCRETING X-RAY PULSARS IN A BROAD ENERGY RANGE

Armin Nabizadeh

OBSERVATIONAL STUDIES OF ACCRETING X-RAY PULSARS IN A BROAD ENERGY RANGE

Armin Nabizadeh

University of Turku

Faculty of Science
Department of Physics and Astronomy
Astronomy
Doctoral Programme in Exact Sciences

Supervised by

Dr. Sergey Tsygankov
University of Turku

Prof. Juri Poutanen
University of Turku

Reviewed by

Prof. Alexis Finoguenov
University of Helsinki

Prof. Josefin Larsson
KTH Royal Institute of Technology

Opponent

Dr. Pablo Reig
Foundation for Research and Technology-Hellas

To my beloved parents, Mehdi and Azam

ABSTRACT

Among all interesting astrophysical objects in the universe, only a few are capable of improving our understanding of physics under extreme conditions. Accreting neutron stars are one of these objects. These compact objects are the collapsed remnants of massive stars which have undergone a supernova explosion in the final stage of their evolution. Some neutron stars are found in binary systems in which they are gravitationally bound to a normal main sequence star. Consequently, a flow of matter from the companion star can be accreted onto the surface of the neutron star. As a result, a substantial fraction of the gravitational energy of infalling matter is converted into a large amount of radiation, mostly in the form of X-rays. These rotating compact objects that emit pulsed beams of radiation along the line of sight of the observer are called X-ray Pulsars.

This thesis is devoted to the observational study of the X-ray emission emerging from the accretion-powered X-ray pulsars. Particularly, four accreting X-ray pulsars, Swift J1816.7−1613, GX 301−2, 4U 1901+03, and 2S 1845−024, observed at various activity levels, i.e. outburst or quiescence, have been studied. The X-ray observations provided by multiple cosmic telescopes such as *NuSTAR*, *XMM-Newton*, *Chandra*, *Swift*, *Insight-HXMT*, and *Fermi* were used. Through X-ray spectral and temporal analyses, I have been able to investigate the emitting regions in more detail and obtain the most important physical properties of the sources such as the magnetic field strength.

The observational results I obtained in the light of this thesis have improved our understanding of the selected X-ray pulsars in high- and low-states. In particular, I demonstrate that even during the strong spin-up episode detected in the wind-accreting X-ray pulsar GX 301−2 the source is still powered by direct accretion from the wind and it is not completely switching to the disk-fed regime as expected. I have also obtained evidence that even in high-luminosity sources, e.g. 4U 1901+03, the observed absorption-like feature around 10 keV may not be attributed to cyclotron lines, but can be an artifact of the two-component spectrum. Moreover, I was able to estimate the magnetic field strength, distance and the type of the optical companions in poorly studied X-ray pulsars Swift J1816.7−1613 and 2S 1845−024 using both X-ray and IR observations.

KEYWORDS: high-energy astrophysics, neutron stars, X-ray pulsars, magnetic fields, spectral analysis

TIIVISTELMÄ

Osa astrofysikaalisista kohteista on erityisen sopivia parantamaan ymmärtämystämme äärimmäisten olosuhteiden fysiikasta. Neutronitähdet ovat yksi esimerkki tällaisista kohteista. Nämä kompaktit kohteet syntyvät supernovaräjähdyksissä massiivisten tähtien kehityksen loppuvaiheessa. Osa neutronitähdistä esiintyy kaksoistähdissä, missä toisena komponenttina on pääsarjan tähti. Tällaisissa systeemeissä neutronitähti voi alkaa "syömään" kumppaniaan ja huomattava osa neutronitähden pinnalle putoavan materian potentiaalienergiasta muuttuu havaittavaksi säteilyksi, lähinnä Röntgensäteilyksi. Kohteita, joissa neutronitähden pyöriminen saa aikaan säännöllisiä säteilypulsseja havaitsijaa kohti sanotaan Röntgenpulsareiksi.

Tässä työssä tutkittiin neljän Röntgenpulsarin, Swift J1816.7−1613, GX 301−2, 4U 1901+03, and 2S 1845−024 Röntgensäteilyä kahdella aktiivisuustasoilla, hiljaisessa vaiheessa ja purkauksessa. Työssä käytettiin havaintoja usealta eri satelliitilta, kuten NuStar, XMM-Newton, Chandra, Swift, Insight-HXMT ja Fermi. Tutkimalla sekä kohteiden spektriä että niiden kirkkaudenmuutoksia pystyttiin yksityiskohtaisesti tutkimaan säteilyalueiden fysiikkaa ja määrittämään niiden tärkeimmät fysikaaliset parametrit kuten magneettivuon tiheys.

Työn ansiosta ymmärrämme nyt enemmän näiden kohteiden fysiikasta sekä hiljaisessa vaiheessa että purkauksessa. Erityisesti tässä työssä osoitettiin, että kohteen GX 301−2 ns. "spin-up" -vaiheessa säteily on pääosin peräisin materiasta, jonka neutronitähti on kerännyt kumppaninsa tähtituulesta, eikä ympäröivästä kertymäkiekosta, kuten olisi odotettavissa. Korkean luminositeetin kohteen 4U 1901+03 tapauksessa saatiin viitteitä siitä, että 10 keV:n energian kohdalla esiintyvä absorptiosignaali ei johdu syklotronisäteilystä, vaan todennäköisesti molempien komponenttien spektrien yhteensekoittumisesta. Lisäksi yhdistämällä Röntgen- ja infrapunahavaintoja pystyin arvioimaan aikaisemmin huonosti tutkittujen kohteiden Swift J1816.7−1613 ja 2S 1845−024 magneettivuon tiheyden, etäisyyden ja komponenttien optiset ominaisuudet.

ASIASANAT: astrofysiikka, neutronitähdet, röntgenpulsarit, magneettikentät, spektrianalyysi

Acknowledgements

Iman Azimi, Yeganeh Fakhrolhasani, Arman Anzanpour, Nilufar Hashempour, Konrad Patyra, Nima Bonyadi, Mohammad Taher Ghalandari, Shirin Sepehri, Vesal Rasoulzadeh, Razieh Zare, Saeed Mehrang, Mostafa Aghajani, Najibeh Farrokh, Mina Shahmoradi, Mohammad Shariat Naseri, Mahdi Moghaddam, Sina Khoshsima and Navid Afzalsoltani. I always feel lucky and happy to have such supportive friends.

I am grateful to the pre-examiners of the thesis, Prof. Alexis Finoguenov and Prof. Josefin Larsson, whose feedback and comments improved the quality of the thesis. Additionally, I would like to thank Dr. Pablo Reig for accepting to be my esteemed opponent.

As a final note, I would like to thank Nasrin, my beautiful and loving wife. She was undeniably the bedrock of my life for the last 13 years because of her support, encouragement, patience, and unwavering faith in me. I appreciate each moment spent with you, and I love you always and forever.

01.10.2022
Armin Nabizadeh

Table of Contents

Abbreviations

ACIS	Advanced CCD Imaging Spectrometer
ARF	Ancillary Response File
BAT	Burst Alert Telescope
BeXRBs	Be/X-ray binaries
CC	Continuous Clocking
CCD	charge-coupled device
CRSF	Cyclotron Resonant Scattering Feature
CV	cataclysmic variables
EPIC	European Photon Imaging Camera
ESA	European Space Agency
FOV	Field of View
FPM	Focal Plane Module
FWHM	Full Width at Half Maximum
GAPP	GBM Accreting Pulsars Program
GBM	Gamma-ray Burst Monitor
GLIMPSE	Galactic Legacy Infrared Midplane Survey Extraordinaire
GRB	Gamma-Ray Burst
HETG	High Energy Transmission Grating
HMXBs	High-Mass X-ray Binaries
HRC	High Resolution Camera
HRMA	High Resolution Mirror Assembly
HXMT	Hard X-ray Modulation Telescope
IR	infrared
IRAC	Infrared Array Camera
ISM	interstellar medium
LAT	Large Area Telescope
LETG	Low Energy Transmission Grating

LMXBs	Low-Mass X-ray Binaries
MCs	Magellanic Clouds
MOS	Metal Oxide Semiconductor
NASA	National Aeronautics and Space Agency
NS	neutron star
NuSTAR	Nuclear Spectroscopic Telescope Array
PC	Photon-Counting
PNS	proto neutron star
RGS	Reflection Grating Spectrometers
RMF	Redistribution Matrix File
SCD	Swept Charge Device
SFXT	Super-giant Fast X-ray Transient
sgXRBs	supergiant X-ray binaries
TE	Timed Exposure
UKIDSS-GPS	UKIRT Infrared Deep Sky Galactic Plane Survey
UKIRT	United Kingdom Infrared Telescope
ULX	Ultraluminous X-ray source
UVOT	Ultraviolet-Optical Telescope
WFCAM	Wide Field Camera
WT	Window Timing
XMM-Newton	X-ray Multi-mirror Mission
XRB	X-ray binary
XRP	X-ray pulsar
XRT	X-Ray Telescope

List of Original Publications

This dissertation is based on the following original publications, which are referred to in the text by their Roman numerals:

I   A. Nabizadeh, S. S. Tsygankov, D. I. Karasev, J. Mönkkönen, A. A. Lutovi-
        nov, D. I. Nagirner, J. Poutanen.
        Properties of the transient X-ray pulsar Swift J1816.7–1613 and its optical
        companion.
        Astronomy & Astrophysics, 2019; 622: A198.

II   A. Nabizadeh,, J. Mönkkönen, S. S. Tsygankov, V. Doroshenko, S. V. Molkov,
        J. Poutanen.
        NuSTAR Observations of the Wind-fed X-Ray Pulsar GX 301–2 During an
        Unusual Spin-up Event.
        Astronomy & Astrophysics, 2019; 629: A101.

III   A. Nabizadeh, S. S. Tsygankov, L. Ji, V. Doroshenko, S. V. Molkov, Y. Tuo,
        S. N. Zhang, F. J. Lu, S. Zhang, J. Poutanen.
        Spectral evolution of X-ray pulsar 4U 1901+03 during 2019 outburst based
        on Insight-HXMT and NuSTAR observations.
        Astronomy & Astrophysics, 2021; 652: A89.

IV   A. Nabizadeh, S. S. Tsygankov, S. V. Molkov, D. I. Karasev, L. Ji, A. A.
        Lutovinov, J. Poutanen.
        Broad-band analysis of X-ray pulsar 2S 1845–024.
        Astronomy & Astrophysics, 2021; 657: A58.

List of publications not included in the thesis

I   A. Nabizadeh, S. Balman.
    X-ray properties of dwarf nova EY Cyg and the companion star using an
    XMM-Newton observation.
    Advances in Space Research, 2020; 5: 1139-1146.

II J. Mönkkönen, V. Doroshenko, S. S. Tsygankov, A. Nabizadeh, P. Abol-
    masov, J. Poutanen.
    Discovery of a retrogradely rotating neutron star in the X-ray pulsar GX
    301–2.
    Monthly Notices of the Royal Astronomical Society, 2020; 494: 2178-2182.

III Y. L. Tuo, L. Ji, S. S. Tsygankov, T. Mihara, L. M. Song, M. Y. Ge, A.
    Nabizadeh et al.
    Insight-HXMT insight into switch of the accretion mode: The case of the
    X-ray pulsar 4U 1901+ 03.
    Journal of High Energy Astrophysics, 2020; 27: 38-43.

IV L. Ji, L. Ducci, A. Santangelo, S. Zhang, V. Suleimanov, S. S. Tsygankov,
    V. Doroshenko, A. Nabizadeh et al.
    Switches between accretion structures during flares in 4U 1901+ 03.
    Monthly Notices of the Royal Astronomical Society, 2020; 493: 5680-5692.

V   MAGIC Collaboration.
    First detection of VHE gamma-ray emission from TXS 1515–273, study of
    its X-ray variability and spectral energy distribution.
    Monthly Notices of the Royal Astronomical Society, 2021; 507: 1528-1545.

VI L. Ji, V. Doroshenko, V. Suleimanov, A. Santangelo, M. Orlandini, J. Liu,
    L. Ducci, S. N. Zhang, A. Nabizadeh et al.
    X-ray reprocessing in accreting pulsar GX 301-2 observed with Insight-
    HXMT.
    Monthly Notices of the Royal Astronomical Society, 2021; 501: 2522-2530.

VII MAGIC Collaboration.
    Testing two-component models on very high-energy gamma-ray-emitting
    BL Lac objects.
    Astronomy & Astrophysics, 2020; 640: A132.

1 A brief history of X-ray pulsars

Whilst the history of astronomy dates back to antiquity, the story of X-ray astronomy has begun more recently in 1946, when the photon counter mounted on a V2 rocket detected the first solar X-ray emission (Friedman et al. 1951). Later, in 1962, the first cosmic X-ray source was discovered by Giacconi et al. (1962)[1] with the Geiger counters onboard an Aerobee sounding rocket. Having located in the constellation Scorpius, the source was later named Sco X-1. The recorded X-ray emission revealed the object to be thousands of times more luminous than the Sun. Further studies identified an optical companion of 13 magnitudes for the system. The physical and orbital parameters pointed to the source (Zeldovich & Guseynov 1966) being a compact object, however, it puzzled astronomers to determine the cause of the steady production of X-ray emission in the long run. As a solution, the concept of the accretion flow onto a compact object was proposed by Hayakawa & Matsuoka (1964) and investigated further by Shklovsky (1967) and Prendergast & Burbidge (1968). Meanwhile, the optical spectral analyses confirmed that Sco X-1 (Westphal et al. 1968) and Cyg X-2 (Lynds 1967) are actually binary systems which vastly supported the accretion scenario. Based on these studies, the X-rays originated in the falling of hot gas ejected from a binary companion onto a compact object. Assuming M and R to be the mass and radius of the object, the potential energy released by accreting a test particle m is defined by

$$E = \frac{GMm}{R} = 1.3 \times 10^{20} \times m \ \text{erg}, \tag{1}$$

where $M = 1.4 M_\odot$ and $R = 10$ km are canonical values for a neutron star (NS) and G is the gravitational constant. Therefore, one gram of accreted matter may release a huge amount of energy. The luminosity, L, produced during mass accretion can be obtained by

$$L = \frac{GM\dot{m}}{R}. \tag{2}$$

Here $\dot{m}$ is mass accretion rate, i.e. the amount of matter accreted on the compact object per unit time. Therefore, an observed X-ray luminosity of $\sim 10^{36}$ erg s^{-1} for a NS with canonical mass and radius (see Sec. 2.1.2), needs a mass accretion rate

---

[1]The 2002 Nobel Prize in physics was awarded to Riccardo Giacconi for "for pioneering contributions to astrophysics, which have led to the discovery of cosmic X-ray sources".
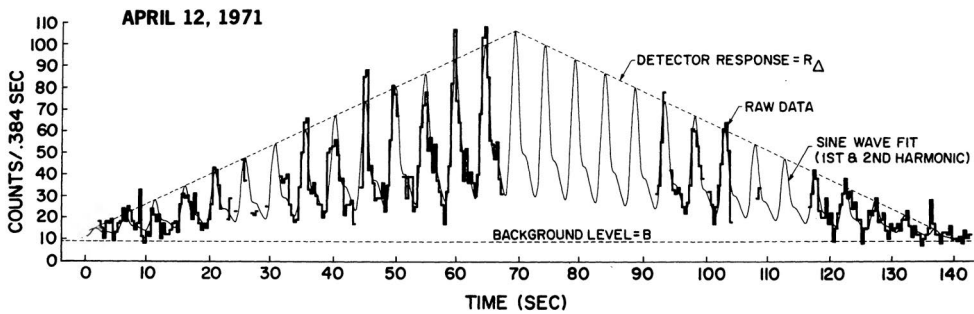
Figure 1. Pulsations from XRPs Cen X-3 with a period of 4.84 s discovered through the *Uhuru* observation of the source. The lightcure modeled with a sinusoidal fit clearly shows the periodic nature of the pulsar. The image is adopted from Giacconi et al. (1971).

of $\dot{m} \sim 10^{15}$ g s^{-1}. Further studies based on optical spectral analysis revealed Sco X-1 is indeed a binary system in which the accreting matter can be transferred to the compact object via accretion disk or directly from stellar wind ejected from the companion or both. Binary systems such as Sco X-1 are known as X-ray binaries (XRBs).

Although the number of discovered X-ray sources reached about 20 by the year 1970, the actual turning point in this area happened in December 1970 with the launch of *Uhuru*, the first X-ray satellite operated by National Aeronautics and Space Agency (NASA). During the first-ever all-sky survey in X-rays, *Uhuru* discovered 339 X-ray sources within a 27-month period (Giacconi et al. 1972; Forman et al. 1978). One of the most significant discoveries of the telescope was the detection of 4.84 s X-ray pulsations from Cen X-3 (see Fig. 1; Giacconi et al. 1971) leading to the identification of the first X-ray pulsar (XRP). Pulsars in general are rotating NS emitting beams of radiation from their magnetic poles. Due to misalignment between their rotation and magnetic field axes, radiation beams reach the observer with a periodic nature, known as the lighthouse effect.

The extreme physical conditions present in the vicinity of NSs such as extreme gravitational forces, high temperatures, and super-strong magnetic fields cause the accretion process in XRPs to release a great deal of energy, primarily in the form of X-rays. Hence these sources provide a unique tool to investigate the physics of matter under extreme conditions which are impossible to attain in terrestrial laboratories. After *Uhuru*, the operation of several other X-ray missions, e.g. *Einstein*, *EXOSAT*, *Ginga*, *ASCA*, *RXTE*, etc., provided the opportunity of performing imaging, temporal and spectral analyses on XRPs which has significantly broadened our knowledge. Particularly, different radiative processes have been proposed to explain the interaction of hot plasma with the strong magnetic field of a NS with $B \sim 10^{12}$ G. Yet, what exactly happens in accreting XRPs is not clear. Hence, the existence

of many unsolved questions makes these systems of great interest to be investigated theoretically and observationally.

The later technological advances in X-ray detectors as well as the launch of multiple X-ray satellites that operate in different energy bands have enabled X-ray astronomy to encompass a wide variety of X-ray sources and phenomena in addition to XRBs, such as cataclysmic variables (CV), supernova remnants, active galactic nuclei, gamma-ray bursts, etc. Although the number of unique X-ray sources reached about 1.25 million in 2017[2], there are only about a hundred confirmed XRPs detected so far (Walter et al. 2015).

The current thesis presents the observational investigations of the selected accretion-powered XRPs using X-ray observations provided by several cosmic satellites. Chapter 2 presents an introduction to NSs, XRBs and different accretion mechanisms. The properties of observed X-ray emission from XRPs are also discussed in this chapter. Chapter 3 provides a short description of the X-ray satellites whose data are used in this thesis. The chapter also gives the basics of X-ray timing and spectral analysis as well as the definition of the commonly used phenomenological models. Chapter 4 contains the summary of the original publications published by the author.

---

[2] https://heasarc.gsfc.nasa.gov/docs/heasarc/headates/how_many_xray.html

2 Physics of accretion powered neutron stars

2.1 Neutron stars

2.1.1 Formation

Soon after the discovery of neutrons in 1932 (Chadwick 1932), Baade & Zwicky (1934) proposed a NS as the ultimate stage of the massive stars evolution. Once stars with masses ~9–25 $M_\odot$ start to fuse heavy elements, an iron-reach core will be reached after several burning stages. At this point, as the core exceeds the Chandrasekhar mass limit (1.44 $M_\odot$) the electron degeneracy pressure is no longer sufficient to support the core from gravitational contraction (Koester & Chanmugam 1990). Hence, sudden collapse takes place and the neutron degeneracy pressure becomes dominant (Bethe et al. 2003). Consequently, a proto neutron star (PNS), i.e. the first phase of the life of a neutron star, is formed. The sudden increase of temperature and density in a collapsing stellar core allows electrons to be captured by protons, so-called inverse β-decay, that converts protons into neutrons. This process produces a huge amount of neutrinos trapped in the newly born dense PNS. Being released at the same time, these neutrinos create a neutrino burst shock propagating outwards (Baron & Cooperstein 1990; Bethe 1990). Consequently, the outer stellar layer is completely disrupted through a supernova explosion leaving a NS behind. It is also believed that the accumulation of accretion mass onto white dwarfs may cause their masses to exceed the Chandrasekhar limit and form a NS. The same procedure would also happen with the merging of two white dwarfs.

30 years after the predictions, the first actual NS was discovered by Jocelyn Bell and Anthony Hewish in 1967 through the observation of radio pulsations from the source PSR 1919+21. Since then, more than 2600 pulsating NS have been detected (Manchester et al. 2005) in a wide energy band from radio to γ-rays.

2.1.2 Basic parameters

NSs are extremely compact objects with densities up to 10^{15} g cm^{-3} (in the center), radii of 10–12 km and masses in the range 1.2–2.0 $M_\odot$ (Gandolfi et al. 2012; Miller & Lamb 2016). They are mostly characterized by their fast rotation, i.e. spin periods, and their enormously strong magnetic fields. Due to the conservation of angular

momentum ($L = 2/5MR^2\omega$) during the core-collapse procedure, the resulted NS is expected to be rapidly rotating. Assuming the radius and the angular velocity of the progenitor core to be R_c and ω_c, then

$$\omega = \omega_c \left(\frac{R_c}{R}\right)^2 , \tag{3}$$

where R is the radius of the remaining NS. Assuming stellar angular velocity (solar) $\omega_c = 2.9 \times 10^{-6}$ rad/s, the canonical NS radius $R = 10$ km, and stellar core radius $R_c \sim 7 \times 10^3$ km, the spin period $P_s = 2\pi/\omega$ would be ~4.5 s. This is in good agreement with the observations that obtained the spin period of NSs spanning from a few milliseconds to few ten seconds (see, e.g., Lyne et al. 1985). If the rotation axis of a NS is misaligned to the magnetic field axis, the observed emission from the hot spots located on the magnetic poles modulates with the spin period. Hence, the folded light curves, i.e. pulse profiles, would give the spin period of the source (Kraus et al. 2003). The spin period evolution depends on whether the NS is isolated or gravitationally bound to a companion star in a binary system in which the accretion may spin-up the pulsar (see Sec. 2.2). In the former case, the pulsar is observed to spin down over time through the loss of rotational kinetic energy at rates $\dot{P} \sim 10^{-22} - 10^{-8}$ s s^{-1}.

The other important characteristic of pulsars is their strong magnetic fields which interactively govern the accretion flow onto the NS producing X-rays in binary systems (see Sec. 2.3). The exact physics of the intense B-field formation is still under debate. However, it is expected that the conservation of magnetic flux ($\Phi = 4\pi R^2 B$) enhances the magnetic field during the core collapse as

$$B = B_* \left(\frac{R_*}{R}\right)^2 , \tag{4}$$

where B_* is the magnetic field of the progenitor star. Assuming stellar radius $R_* \sim 7 \times 10^5$ km and $B_* \sim 10^3$ G, the B-field strength for a young NS would be $B \sim 5 \times 10^{12}$ G. This is perfectly consistent with the values obtained by direct measurements of B-field strength through the observations of cyclotron absorption lines in XRPs (see Sec. 2.4.2). The emitted energy from pulsars can either be powered by accretion, rotation, or magnetic field decay. As this thesis focuses on the accretion-driven XRPs, the parameters of the other two mechanisms will not be discussed here.

2.2   X-ray binaries

XRBs are gravitationally bound binary systems containing a compact object and an optical companion corotating around their center of mass. The compact object in these systems can be a black hole, a NS, or a white dwarf which accretes matter from the companion star (Nagase 1989; Lewin et al. 1997). The infalling matter releases

Figure 2. Schematic view of LMXBs. The companion (M_1) fills its Roche lobe leading the matter to be steadily transferred to the gravitational potential well of the NS (M_2) via L_1 point. In this procedure, an accretion disk forms around the NS due to the conservation of angular momentum.
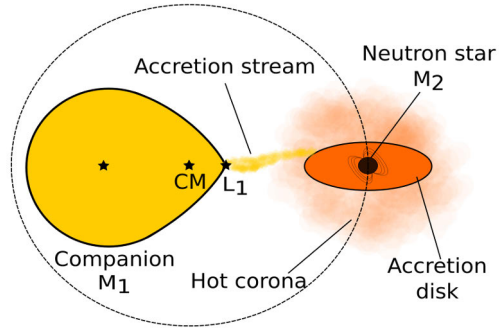
its gravitational potential energies as X-rays, through different radiative processes (see Sec. 2.4.1), making these systems to be the brightest objects in the X-ray regime with luminosities 10^{32}–10^{41} erg s^{-1}, where the brightest ones associated with the recently discovered Ultraluminous X-ray sources (ULXs; Long & van Speybroeck 1983; Fabbiano 1989; Colbert et al. 2004)[1].

XRBs are also categorized in two subclasses: Low-Mass X-ray Binaries (LMXBs) and High-Mass X-ray Binaries (HMXBs) based on the mass and the evolutionary state of companion stars. From now on, only XRBs with a NS as their compact object are of interest in this chapter.

2.2.1 Low-mass X-ray binaries

LMXBs are relatively old systems that contain a low-mass main-sequence star as their optical companion (also known as donor star). The donors with masses typically in ranges $\lesssim$ 1–2 $M_\odot$ are not associated with strong stellar outflows. Hence, mass accretion in LMXBs takes place via the so-called Roche lobe overflow through the first Lagrangian point L_1 in which the gravitational forces of two masses balance each other. Mass transfer via Roche lobe overflow, in general, happens when the optical companion starts to evolve and expand or the binary orbit shrinks. In this case, the star eventually fills its Roche lobe allowing the matter to overflow steadily and continuously towards the compact object's gravitational well (see Fig. 2). The accretion stream carries a large amount of angular momentum. Hence, the conservation of angular momentum leads the matter to orbit circularly around the compact object forming an accretion disk.

As the *B*-field is relatively weak in these systems, no regular X-ray pulses are detected from the majority of these classes of sources. Instead, although the accretion is dynamically stable, X-ray outbursts occur due to the thermonuclear fusion

---

[1] Both NSs and black holes are candidates to contribute in explaining these systems.

Figure 3. Sketch of wind-fed supergiant X-ray binaries in which the orbiting NS (M_2) is embedded in the stellar wind. The interaction of supersonic stellar wind with the moving NS results in a bow shock in the vicinity of the NS which forms a high density accretion wake behind the compact object (Blondin et al. 1990).
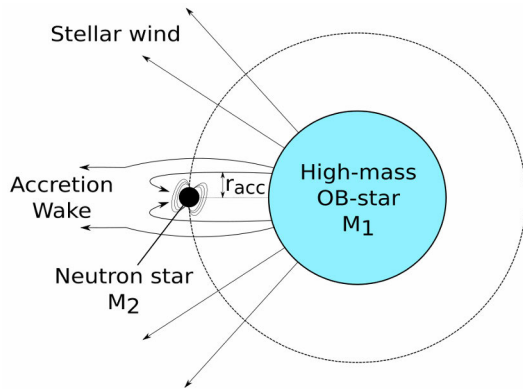
of accreted matter on the surface of NS. The formation of such systems is not fully understood. However, the sufficiently low number of detected LMXBs, i.e. less than 200 sources in our galaxy (Liu et al. 2007), points to the specific conditions required for these binaries to be formed. As the mass of the progenitor of NS needs to be of $\gtrsim 8\ M_\odot$, the initial binary should have contained a massive star and a low-mass companion. In addition, LMXBs are close systems where the separation of the binary components is in the range 0.1–$10 R_\odot$ (Brandt & Podsiadlowski 1995; Tauris & van den Heuvel 2006). It is also expected that the system loses more than half of its mass during the supernova explosion. In this case, the binary system can become unbound as the NS undergoes a strong kick (Bhattacharya & van den Heuvel 1991). If the binary remains bound, the kick will transfer momentum to the system's center of mass, allowing it to move. This together with the fact that the LMXBs are old systems explains their wide distribution with regard to the galactic plane (see Fig. 1 in Grimm et al. 2002). The study of X-ray properties in LMXBs is beyond the scope of this thesis, therefore, no further discussion is given here.

2.2.2 High-mass X-ray binaries

HMXBs, on the other hand, host early O–B type high-mass optical companions with masses $\gtrsim 8\ M_\odot$(Bhattacharya & van den Heuvel 1991; Lewin et al. 1997; Kretschmar et al. 2019). Since these stars are short-lived (ages $\lesssim 10^7$ years), HMXBs belong to the youngest stellar population. According to Liu et al. (2006), there are 114 HMXBs detected in Milky Way concentrated towards the galactic plane away from the center, and 128 in the Magellanic Clouds (MCs). It is expected that during binary evolution, the progenitor of the NS with masses $\gtrsim 20\ M_\odot$ expands to fill its Roche lobe transferring most of the hydrogen-rich mass into the companion star of masses $\sim 10\ M_\odot$ (see Hilditch 2001). Consequently, a helium-rich star would be left behind, causing the mass ratio to be inverted. Once the prior star undergoes a supernova explosion, the remaining NS would accrete from the companion.

The accretion process in HMXBs occurs mostly due to strong stellar wind emerging from the companion, and Roche lobe overflow is less common. Unlike the normal stars, O and B supergiants possess an intense stellar wind with high mass-loss rates up to $\dot{M}_{wind} \gtrsim 10^{-7} - 10^{-5}~M_{\odot}~yr^{-1}$ and supersonic velocities of $v_w \sim 1000$ km/s (see Martínez-Núñez et al. 2017, for a review). As shown in Fig 3, the NS is orbiting the companion at very close distances leading the NS to be embedded deeply in the stellar wind. The mass accretion onto the NS occurs in a cylindrical radius (see Fig. 3), the so-called accretion radius. As the binary separation is much larger than the accretion radius, only a small fraction of the total wind of the companion will be accreted on the NS (Martínez-Núñez et al. 2017). Consequently, assuming a spherically symmetric mass loss from the companion ($\dot{M}_{wind}$) and the binary separation of a, the accretion rate onto the NS can be calculated as (Davidson & Ostriker 1973)

$$\dot{M} = \frac{\pi r_{acc}^2}{\Omega a^2} \dot{M}_{wind}, \tag{5}$$

where the solid angle Ω is equal to 4π for isotropic outflow of the stellar wind. The final resulting X-ray luminosity from the process of wind-fed accretion can be given by Eq. (2). As the observed X-ray light curves of these systems are extremely variable, the clumpy wind structure (i.e. a population of dense blobs) was first proposed by Sako et al. (2003). Later, the evidence of such structures was detected in Vela X-1 (Martínez-Núñez et al. 2014) and GX 301–2 (Fürst et al. 2011).

The majority of HMXBs contain a rotating highly magnetized NS as the compact object with a dipole magnetic field strengths of 10^{11}–10^{13} G (Staubert et al. 2019). The strong B-field on the surface of the NS will restrict the accumulation of falling matter into a small area, i.e. the hot spots, preventing the occurrence of thermonuclear bursts in these systems. Instead, they show persistent X-ray pulsations. HMXBs possess a hard X-ray spectrum with kT larger than 15 keV. The evolution of a HMXB can be linked to the formation of a double NS system right after the companion goes through a supernova explosion.

As already mentioned, in LMXBs, disk accretion is the primary mechanism of accretion, and only a small percentage of HMXBs is confirmed to have an accretion disk. Among HMXBs, Cen X-3 (Tjemkes et al. 1986), LMC X-4 (Heemskerk & van Paradijs 1989), and SMC X-1 (Hutchings et al. 1977) are such well-known disk-fed XRPs which are persistent X-ray emitters with high luminosities in the range 10^{37}–10^{38} erg s^{-1}. Moreover, recent theoretical studies (El Mellah et al. 2019; Karino et al. 2019) show that temporary accretion disks can be formed in wind-fed sources under certain circumstances, e.g. for slow stellar wind. In particular, one explanation for sudden spin-up episodes in XRPs is the formation of temporary accretion disks, although it has not yet been confirmed observationally (see, e.g., Nabizadeh et al. 2019). This process can be explained as the substantial angular momentum carried by accretions flow, so a disk-accreting matter can imply stronger accelerating torque
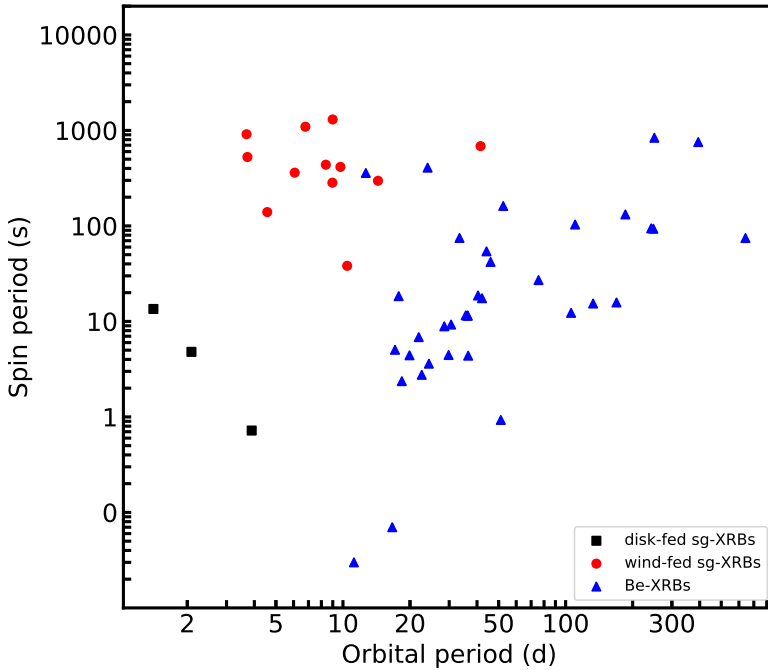
Figure 4. Corbet's diagram (P_{spin} versus P_{orb} of NSs) of all HMXBs in the Milky Way and Magellanic Clouds showing three distinct regions: black squares show disk-fed supergiant XRBs, red circles show wind-fed supergiant XRBs and blue triangles show Be-XRBs. Orbital and spin periods are taken from Townsend et al. (2011) and Kretschmar et al. (2019).

to the compact object (see, e.g., Soker 2004).

Based on the luminosity and the accretion mechanism, HMXBs are broadly divided into three subclasses: disk-fed supergiant X-ray binaries (sgXRBs), wind-fed sgXRBs and Be/X-ray binaries (BeXRBs) which contain a Be type star as their companion. In spite of the fact that all three subclasses are evolved from OB stars commonly found in the Galactic plane and Magellanic Clouds, they differ in the accretion procedure that is responsible for the observed X-rays. Wind-fed sgXRBs are the second most frequent subclass in which the accretion occurs through the stellar wind. High-mass companions in sgXRBs possess a dense and sufficiently slow stellar wind, radially outflowing from the equator, which can be directly captured by the orbiting NS and converted to X-rays. Disk-fed sgXRBs, which represent a small fraction of HMXBs, are persistent X-ray sources that accrete matter through Roche-lobe overflow. Consequently, the corresponding NS can spin up to significantly short spin periods. The most common HMXBs are BeXRBs in which accretion occurs through the interaction between the compact star and the decretion disk around the optical companion.

Figure 5. Schematic diagram of a BeXRB in which the NS is moving on a highly eccentric orbit around the Be-type companion. Once the NS is getting close to the (probably) misaligned circumstellar disk near the periastron, the matter can be accreted onto the NS from the disk causing Type I outbursts.
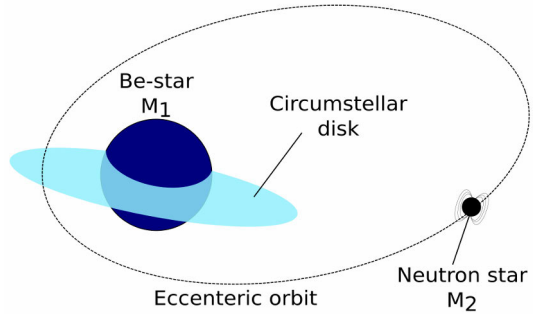
Since most of the HMXBs have a NS as their compact object, the various sub-classes of these systems can be compared through the so-called Corbet's diagram (Corbet 1986). The diagram is obtained by plotting the known spin and orbital periods of the orbiting NSs in HMXBs (see Fig. 4). As shown in the figure, Corbet (1986) discovered that each subclass of the binaries occupies a distinct region in the P_{spin}-P_{orb} diagram emphasizing that there is a considerable connection between various accretion processes and the spin and orbital periods of the system. To be more specific, sgXRBs have short spin and orbital periods with no obvious correlation; while BeXRBs are distributed in the regions with short spin and orbital periods to the regions with long spin and orbital periods roughly following a positive correlation between P_{spin} and P_{orb}.

It is worth mentioning that there is another sub-class of HMXBs, Super-giant Fast X-ray Transients (SFXTs), recently discovered by *INTEGRAL* observatory (Sguera et al. 2005). The accretion in SFXTs is due to a clumpy stellar wind emerged from OB-stars, however, unlike the wind-fed sgXRBs, SFXTs are low-luminous systems exhibiting short and bright flares which last a few hours.

2.2.3   Be phenomenon

As it can be inferred from Corbet's diagram, about two-thirds of all HMXBs belong to the subclass of BeXRBs. In these binaries, the donor is a B-type star showing emission lines of Hydrogen (mostly Hα) in their optical spectrum (Reig 2011). Therefore, the letter "e" in Be distinguishes these stars from the normal B-stars. The line emission and a strong infrared excess are attributed to the presence of a circumstellar disk (see Fig. 5) along the equatorial plane of the star known as a decretion disk (Porter & Rivinius 2003). The formation of such disks is still not fully understood, however, one possible explanation could be the rapid rotation of Be stars at velocities close to the break-up velocity of the star (Rivinius et al. 2013).

The compact object in BeXRBs is mostly a NS that orbits the companion in a

wide and highly eccentric orbit (e ≳ 0.1) leading to very long orbital periods of tens to hundreds of days (see Fig. 4). Due to the presence of the disk, the stellar wind in Be stars is highly anisotropic causing the wind accretion into the compact object to be significantly reduced in comparison to the supergiants or stopped. Hence lower X-ray luminosity emerges from the NS star in these systems especially when it is in orbital phases far away from the periastron. In this case, the source is in the so-called quiescent state. There are two types of outbursts in BeXRBs interrupting the quiescent state: normal outbursts (type I) and giant outbursts (type II).

Close to the periastron, the NS may accrete matter from the Be decretion disk through the Roche lobe overflow. This leads to a sudden increase in the X-ray luminosity reaching $L_X \sim 10^{36-37}$ erg s^{-1}. Outbursts of this type are known as type I outbursts. These outbursts last only about 20–30% of the orbital period emphasizing the transient nature of these sources. Type I outbursts are expected to be regularly happened in highly eccentric systems (Okazaki & Negueruela 2001), e.g. as GRO J1008–57 (Kühnel et al. 2013) and 2S 1835−024 (Finger et al. 1999; Nabizadeh et al. 2022). Type II outbursts, on the other hand, are more complicated and stronger than type I outbursts and are not associated with any specific orbital phases. During type II outbursts the X-ray luminosity can reach over the Eddington limit ($L_X \sim 10^{38}$ erg s^{-1}), e.g. SMX X-3 (Tsygankov et al. 2017a) and Swift J0243.6+6124 (Liu et al. 2022) with luminosities >10^{39} erg s^{-1}. These unpredictable outbursts can last up to or longer than one orbital period. Although the actual cause of Type II outbursts is not fully clear yet, the recent studies suggest that a processing warped disk may be associated with these giant outbursts (see Okazaki et al. 2013; Moritani et al. 2013).

2.3 Accretion onto highly magnetized neutron stars

2.3.1 Magnetospheric boundary

The highly ionized accretion flow would be disrupted by the strong magnetic field of NS at a certain distance ($\sim 10^8$ cm) away from the object, so-called magnetospheric radius R_M. At magnetospheric radius, the pressure of the infalling matter is in equilibrium with the magnetic pressure. The interaction of the accretion flow with the NS magnetic field is governed by complicated physics depending on many factors such as plasma instabilities, perturbations in the accretion disc, specific parameters of the NS, torques, and other parameters (see Lai 2014, for a review). However, still, a simplified picture of such interactions can be determined by investigation of the equilibrium between the magnetic and plasma pressures. Considering a spherically symmetric accretion flow with free-fall velocity for simplicity, by equating the ram pressure of the infalling matter

$$P_{\mathrm{ram}} = \frac{1}{2}\rho v^2 \sim \frac{\dot{M}}{4\pi}\left(\frac{GM}{2r^5}\right)^{\frac{1}{2}} \tag{6}$$

with the magnetic field pressure

$$P_{\mathrm{mag}} = \frac{B^2}{8\pi} = \frac{1}{8\pi}\frac{\mu^2}{r^6}, \tag{7}$$

where μ is the dipole magnetic momentum and r is a distance from NS, the so-called Alfvén radius is derived. Consequently, the Alfvén radius at which the equilibrium is approached, is defined as

$$R_{\mathrm{A}} = 3 \times 10^8 \dot{M}_{17}^{-2/7} \mu_{30}^{4/7} (M_{1.4})^{-1/7} \mathrm{cm}, \tag{8}$$

where the $\dot{M}$ and μ are given in unites of 10^{17} g s^{-1} and 10^{30} G cm^3, respectively, and $M_{1.4}$ is the NS mass in units of $1.4M_\odot$. Having the Alfvén radius, one can define the actual magnetospheric radius as $R_{\mathrm{M}} = \Lambda R_{\mathrm{A}}$, where the coefficient Λ depends on the accretion geometry. In case of disc accretion $\Lambda = 0.5$, while for spherical accretion $\Lambda \approx 1$ (Ghosh & Lamb 1978, 1979). The magnetosphere rotates with the same angular velocity as the NS while the inner disk plasma is expected to be rotating at local Keplerian velocity. At a certain distance, known as the co-rotating radius, the angular velocity of the magnetosphere would be equal to the Keplerian angular velocity of the inner disk matter:

$$R_{\mathrm{co}} = \left(\frac{GMP^2}{4\pi^2}\right)^{1/3} \mathrm{cm}, \tag{9}$$

where P is the spin period of the NS. At low mass accretion rate, two scenarios are expected depending on the relative sizes of the magnetospheric radius (R_{M}) and the co-rotating radius. If the angular velocity of the magnetosphere is smaller than the Keplerian velocity of the inner disk, i.e. $R_{\mathrm{M}} < R_{\mathrm{co}}$, the matter is allowed to be accreted onto the surface of NS producing X-ray radiation (see sec. 2.3.2). On the contrary case, i.e. $R_{\mathrm{M}} > R_{\mathrm{co}}$, the falling matter is thrown away by the centrifugal barrier and no accretion occurs. This situation is known as the propeller effect (Illarionov & Sunyaev 1975; Ustyugova et al. 2006) in which the accretion flow stops at $R_{\mathrm{M}} = R_{\mathrm{co}}$. Hence, the limiting mass accretion rate can be calculated as

$$\dot{M}_{\mathrm{lim}} \approx 3.75 \times 10^{17} \Lambda^{7/2} B_{12}^2 P^{-7/3} M_{1.4}^{-5/3} R_6^6 \text{ g s}^{-1}, \tag{10}$$

where $M_{1.4}$ and R_6 are the NS mass and radius in units of $1.4M_\odot$ and 10^6, respectively, determines the source transition to the propeller regime. This can be translated to the corresponding X-ray luminosity

$$L_{\mathrm{lim}} \approx 5 \times 10^{37} \Lambda^{7/2} B_{12}^2 P^{-7/3} M_{1.4}^{-2/3} R_6^5 \text{ erg s}^{-1}, \tag{11}$$

where the magnetic field B is given in the units of 10^{12} G. The transition to the propeller regime is found in several XRPs (Campana et al. 2001; Tsygankov et al. 2016; Lutovinov et al. 2017).

Figure 6. Schematic view of accretion column formed above the polar caps of NS. In the thermal mound soft seed photons (red) are produced through the thermal radiation (blackbody) and in the column by bremsstrahlung and cyclotron emissions. These photons interact with infalling supersonic accretion flow via bulk Comptonization and get up-scattered to higher energies. The image is adopted from Becker & Wolff (2007).
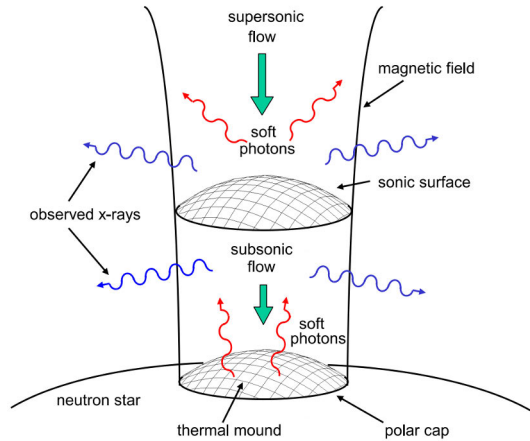
If the spin period of an XRP is long enough, the outburst decay may not end up in the propeller regime, but rather, the source continues to accrete stably from a cold low-ionization disk. In a cold recombined disk, where the effective temperature is below 6500 K, the viscosity and thus the accretion rate is low (Lasota 2001),

$$\dot{M} < \dot{M}_{\rm cold} \approx 3.5 \times 10^{15} r_{10}^{2.65} M_{1.4}^{-0.88} \text{ g s}^{-1}, \tag{12}$$

where r_{10} is the inner disk radius in units of 10^{10} cm. By substituting the magnetospheric radius into Eq. (12), the luminosity that corresponds to the transition to the cold disk is obtained as

$$L < L_{\rm cold} \approx 9 \times 10^{33} \Lambda^{3/2} B_{12}^{0.86} M_{1.4}^{0.28} R_6^{1.57} \text{ erg s}^{-1}. \tag{13}$$

A longer spin period results in a lower centrifugal barrier, which is crucial to switching the accretion disk to the cold state before transitioning into the propeller regime. Consequently, the final state the source enters after an outburst can be determined by the spin period and magnetic field of the NS (Tsygankov et al. 2017b). By equating $L_{\rm lim}$ and $L_{\rm cold}$, the critical value for the spin period as a function of the magnetic field is derived as

$$P^* = 36.6 \, \Lambda^{6/7} B_{12}^{0.49} M_{1.4}^{-0.17} R_6^{1.22} \text{ s}. \tag{14}$$

For sources with $P > P^*$, the source ends up accreting from the cold disk, e.g., GRO J1008−57 (Tsygankov et al. 2017b). Otherwise, the source will enter the propeller regime.

2.3.2 Accretion column

At $r \sim R_{\rm M}$, the accretion flow penetrates into the magnetosphere and gets accelerated along the B-field lines onto the polar caps. Near the surface of NSs, the medium is

dominated entirely by the strong magnetic field. As a result, a column-like structure, the so-called accretion column (see Fig. 6), is formed close to the stellar surface. The geometrical structure of the accretion column is influenced by the mass accretion rate (Mushtukov et al. 2015b) and B-field structure in the vicinity of the NS surface (Brice et al. 2021). The base of the accretion column, the so-called thermal mound, is the place where accreting matter lands. The seed photons produced via different processes in the accretion mound and column (see Sec. 2.4.1) are up-scattered to higher energies through the interactions with the infalling supersonic accretion matter. The geometry of the accretion column is shown in Fig. 6. The radius of the thermal mound can be roughly estimated to be $\sim 0.1 R_{NS} \sim 1$ km (Davidson & Ostriker 1973). The shape of this region depending on the accretion mechanism can be a filled circle in the case of wind accretion or a ring-like structure in the case of disk accretion (see Mészáros 1984, on possible accretion column geometries).

Matter accreting on the top of NS polar caps is decelerated through different mechanisms, depending on the accretion rate. At low accretion rates, the infalling flow gets decelerated either in the NS atmosphere via Coulomb collisions (Basko & Sunyaev 1975; Staubert et al. 2007; Becker et al. 2012) or on top of the the collisionless shock above the surface (Langer & Rappaport 1982; Bykov & Krasil'shchikov 2004). In this regime, a thermal hot spot is formed at the stellar surface which is the source of X-ray emissions. In the case of high mass accretion rates, the radiation pressure increases in the opposite direction of the falling matter, leading to the accretion stopping at some height above the NS surface in a radiation-dominated shock (Basko & Sunyaev 1976).

The transition between these two regimes strongly depends on the mass accretion rate. Therefore, Basko & Sunyaev (1976) introduced a critical luminosity L_{crit}, to differentiate these states as sub- and supercritical regimes. In the sub-critical regime, $L < L_{crit}$, when the accretion rate is low, the X-ray photons produced in the mound can escape along the magnetic field lines, through the optically-thin medium on top of the mound, in a *pencil-beam* pattern (Fig. 7-right). In the super-

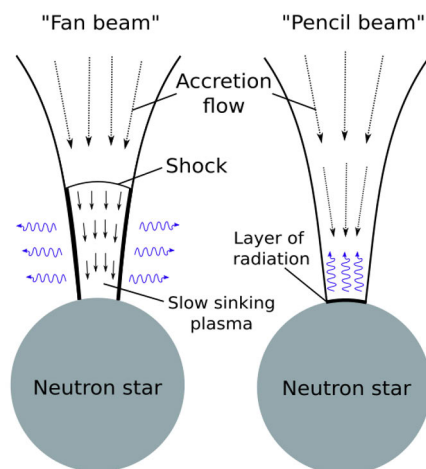**Figure 7.** A sketch of accretion column at different accretion regimes. In the sub-critical regime (right) the produced X-rays can escape along the B-field lines in a pencil-beam pattern. In super-critical regime (left), the X-ray photons can only escape the column perpendicularly forming a fan-beam pattern. See the text for more detail. The image is adapted from Kretschmar (1996)

critical regime, $L > L_{crit}$, the optically-thick shock front does not permit the photons to be upscattered vertically, thus, the photons can only be emitted perpendicular to the accretion column in a *fan-beam* pattern (Fig. 7-left). Switching from pencil-beam to fan-beam pattern is expected to be detected as a phase shift in the observed pulse profile. Moreover, the pulse profile in the super-critical regime tends to be more complex than the one in the sub-critical. In particular, once the accretion column is formed, a fraction of fan-beam emission is expected to be intercepted and reproduced by the NS surface in the vicinity of the column (Poutanen et al. 2013) which has effects on both the spectra (Postnov et al. 2015) and pulse profile formation (Lutovinov et al. 2015; Mushtukov et al. 2018). Additionally, gravitational light bending also affects the shape of pulse profiles (Riffert & Meszaros 1988; Beloborodov 2002; Poutanen & Beloborodov 2006).

Recent theoretical studies based on different approaches (Becker et al. 2012; Mushtukov et al. 2015b) estimated the L_{crit} to be around 10^{37} erg s^{-1}. However, at high accretion rates, the interactions of matter and radiation, especially in a strong magnetic field, are even more complex. Estimations suggest that for sources with magnetar-like magnetic fields ($B > 10^{14}$) and long spin periods, the L_{max} can be as high as 10^{40} erg s^{-1} (Mushtukov et al. 2015a). This may explain the extreme luminosities produced by ULXs (Bachetti et al. 2014; Israel et al. 2017).

2.4 Emission from accreting X-ray pulsars

2.4.1 Continuum X-ray emission

The observations show that the X-ray continuum of accretion-powered XRPs can be described with an absorbed power-law model modified by an exponential cut-off, mostly at 10–30 keV. Most XRPs also represent emission lines, e.g. iron emission lines (see Sec. 2.4.4), and absorption features, e.g. cyclotron absorption lines (see Sec. 2.4.2), in their spectra. Some sources also show deviations at lower energies < 5 keV which can be taken into account by a blackbody component (see Sec. 2.4.5). Several analytical and numerical attempts have been carried out to develop a theoretical model to reproduce the shape of observed XRPs spectra (Nagel 1981b,a; Meszaros et al. 1983; Meszaros & Nagel 1985; Burnard et al. 1988, 1991; Becker 1998; Becker & Wolff 2005b). However, there is still no a self-consistent model applicable to X-ray spectra emerging from a wide range of accretion luminosities. This is due to the complexity of physical processes taking place in the accretion column structured with a strong magnetic field. The current knowledge of spectral formation in these systems is based on the theoretical studies by Becker & Wolff (2005a,b); Becker & Wolff (2007).

Becker & Wolff (2007) proposed a theoretical model which successfully reproduced the X-ray spectra of several bright XRPs such as Her X–1, Cen X–3, and LMC

Figure 8. Theoretical X-ray spectrum of LMC X-4 (red). The spectrum consists of bremsstrahlung (green), cyclotron (blue) and blackbody (black) components together with an iron emission line (pink). The X-ray spectrum obtained with *BeppoSAX* (black dots; La Barbera et al. 2001) is shown for comparison. The plot is adopted from Becker & Wolff (2007).
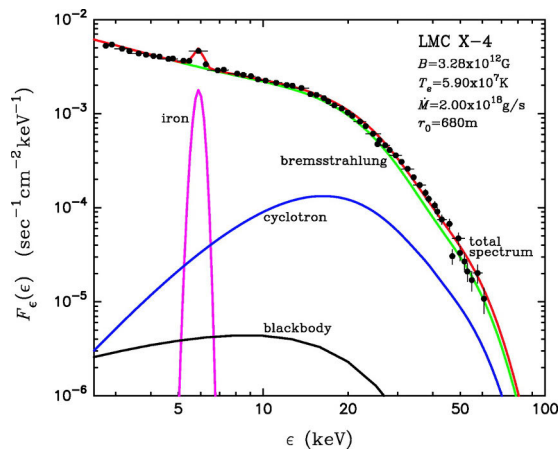
X–4. In this model, the seeds photons are produced by three different mechanisms: at the thermal mound via blackbody radiation and inside the accretion column via bremsstrahlung radiation, i.e. electrons emit photons as they are deflected by ions in the infalling plasma, and cyclotron emission (see Fig. 6). As a result of the strong magnetic field lines, electron energy is quantized into Landau levels, which results in photon emission when the electrons are de-excited from higher to lower levels. The produced seed photons then get up-scattered to high energies through bulk and thermal Comptonization. The term bulk Comptonization refers to the inverse Compton scattering of photons by the relativistic electrons coming from the bulk motion of the infalling plasma. This process takes place through the radiation-dominated shock in the accretion column where the accretion flow is significantly decelerated. In the framework of the model proposed by Becker & Wolff (2007), the power-law shape of the X-ray spectrum is mostly due to the bulk Comptonization. However, thermal Comptonization is responsible for the cut-off at the hard part of the spectrum and a flattening at the soft part.

An example of the theoretical X-ray continuum based on this model is shown in Fig. 8 which is computed for the XRB LMC X-4 in comparison to the *BeppoSAX* X-ray spectrum of the source. The total spectrum is produced using three radiation components blackbody, cyclotron, and bremsstrahlung radiations together with an iron emission line component at 6.4 keV. Although the model is available in fitting packages for public use, the number of free fit parameters makes it problematic to use. Despite the fact that in the last decade, the model has been developed describing sources with high mass accretion rates (Farinelli et al. 2012, 2016; Wolff et al. 2016), it still requires improvement to account for spectra obtained in a broad range of luminosity (see e.g. Ferrigno et al. 2009). Meanwhile, other available phenomenological models are widely used to model the observed X-ray spectra of XRPs (see Sec. 3.2.2).

At very low luminosities, it is expected that systems will have a simple form of emission region which is not affected by several complex mechanisms associated with the accretion column. However, the production of high-quality observations at low luminosities which became available only recently, revealed the spectrum of some sources, e.g. X Per (Di Salvo et al. 1998), A 0535+262 (Tsygankov et al. 2019a) and GX 304−1 (Tsygankov et al. 2019b), can deviate significantly from the standard picture by showing two distinct humps. Di Salvo et al. (1998) proposed a double-component spectral model to describe such spectrum of X Per which alternatively was also interpreted as a broad cyclotron line (Coburn et al. 2001; Lutovinov et al. 2012). Based on the initial scenario by Nelson et al. (1995), Tsygankov et al. (2019b,a) concluded that the hard component of the double-hump spectrum may be associated with the emission of cyclotron photons at the top layer of the atmosphere. These photons are produced through the recombination of electrons collisionally excited to the upper Landau levels and further being Comptonized by hot electron gas (Mushtukov et al. 2021; Sokolova-Lapa et al. 2021).

2.4.2 Cyclotron resonant scattering feature

The X-ray spectra of several accreting XRPs are featured by narrow absorption-like structures mostly at ~10–90 keV known as Cyclotron Resonant Scattering Features (CRSFs) or shortly as cyclotron lines. Such features were first discovered in the spectrum of Her X-1 (Truemper et al. 1978) and since then have been detected in more than 40 sources Staubert et al. (2019), thanks to the launch of broadband X-ray telescopes, e.g. *NuSTAR* (see Sec. 3.1.1). As already mentioned, in the presence of a strong magnetic field of orders 10^{12} G, the energy state of the free electrons in the infalling plasma are quantized to discrete Landau levels (Lai 2001). The energy of the electrons in each Landau level is given by

$$E_\mathrm{n} = \frac{m_\mathrm{e}c^2}{\sin^2\theta}\left(\sqrt{1 + 2n\frac{B}{B_\mathrm{crit}}\sin^2\theta} - 1\right),\tag{15}$$

where m_e is the mass of electron, θ is the angle between the photon momentum and the magnetic field axis, $n \in \mathbb{N}$ is the Landau level number and the critical magnetic field $B_\mathrm{crit} = \frac{m_\mathrm{e}c^3}{e\hbar} = 4.414 \times 10^{13}$ G (with $\hbar = h/2\pi$ is the Planck's constant; Canuto & Ventura 1977). At lower ranges of magnetic fields, $B \ll B_\mathrm{crit}$, where the magnetic field of most XRPs are lie in, the cyclotron line energy corresponding to the energy difference between Landau levels n and $n+1$ is

$$E_\mathrm{cyc} = \frac{\hbar e}{m_\mathrm{e}c}nB = 11.6\,\mathrm{keV}\,B_{12}\,n,\tag{16}$$

which is known as *12-B-12* rule yielding the fundamental cyclotron line energy ($n = 1$) and its harmonics ($n \geq 2$). In the presence of a strong gravitational potential of the NS, the cyclotron energy is redshifted by z~0.3 (for the canonical mass
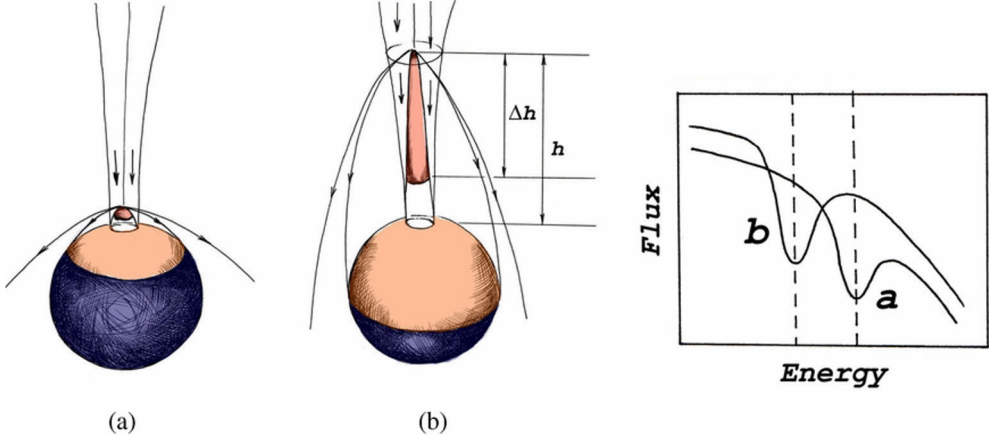
Figure 9. Schematic for the height of accretion column at low (a) and high (b) mass accretion rates. As shown, the illuminated fraction of the NS surface depends on the height of accretion column. The higher intercepted radiation fraction will cause the lower CRSF as the averaged surface magnetic field strength is smaller. Adopted from Poutanen et al. (2013).

and radius of NS), hence Eq. (16) is modified as $E_{\mathrm{cyc}}^{\mathrm{obs}} = E_{\mathrm{cyc}}(1 + z)^{-1}$ with z as the gravitational redshift. In the X-ray spectrum, the absorption of photons in the electron excitation to higher Landau levels manifests itself as absorption-like features around the cyclotron energies, nE_{cyc}. Hence, it provides a direct method to measure the magnetic field strength of an accreting NS, i.e. using Eq. (16). Due to the complexity of cyclotron line formation in the accretion column, no accurate theoretical model has been developed yet and a simple Gaussian absorption profile is used to fit these structures (see Sec.3.2.2).

As already discussed in Sec. 2.3.2, the variations in mass accretion rate and luminosity result in changes in accretion regimes in XRPs. This causes the cyclotron line centroid energy to vary correspondingly with the changes (Becker et al. 2012, and references therein). In particular, sources in the subcritical regime (e.g. Her X-1 and GX 304−1) show a positive correlation between CRSF centroid energy and the X-ray luminosity (Staubert et al. 2007; Vasco et al. 2011; Klochkov et al. 2012; Rothschild et al. 2017; Chen et al. 2021). This can be related to the height of collisionless shock formation which is anticorrelated with the mass accretion rate (Staubert et al. 2007). In contrast, the XRPs in supercritical regimes (e.g. V 0332+53 and 4U 0115+63) show a negative correlation (Mihara et al. 2004; Tsygankov et al. 2006; Nakajima et al. 2006; Tsygankov et al. 2007). This can be explained by the formation of radiation-dominated shock at the accretion column which is the potential region for cyclotron absorption line formation. The height of the radiation-dominated shock is positively correlated with the mass accretion rate. Since $B \propto r^{-3}$, the higher mass

accretion rates lead the line-forming region to be located in lower magnetic field regions. Another possibility for the negative correlation is that the fraction of X-ray emission which is intercepted by the surface of NS (see Sec. 2.3.2) may play a role in forming an absorption-like feature at the cyclotron energy associated with the local magnetic field as shown in Fig. 9 (Poutanen et al. 2013).

2.4.3   Photoelectric absorption

The intrinsic X-ray spectrum that emerged from the NS would not reach the observer untouched. Particularly, the electromagnetic radiation inevitably interacts with neutral/ionized matter located in the vicinity of the NS, e.g. stellar winds from the companion star, or/and in the interstellar medium (ISM), e.g. molecules, and dust. These interactions cause the X-ray spectrum to lose some of its characteristics or/and gain new features as discussed below.

X-ray photons with energies 0.1–10 keV, can be absorbed by atoms or ions, in the line of sight to the observer, resulting in the ejection of a bound electron. The kinetic energy of this electron is equal to $h\nu - E_b$, where $h\nu$ is the photon energy and E_b is binding energy of the electron. This process that is known as photoelectric absorption (or photoabsorption) can occur in atomic and molecular gas and grains. The cross-section for photoelectric absorption is roughly proportional to ν^{-3}, therefore, the absorption happens mostly at low-energy X-rays. One should note that the energy-dependent cross-section $\sigma(E)$ depends strongly on the atomic number of the elements (Wilms et al. 2000). Hence, the X-ray absorption strongly depends on both the abundance of elements and the elemental cross-sections. The total cross-section can be normalized to the total hydrogen number density, N_H, which is the number of absorbing atoms per unit cross-sectional area (atoms cm^{-2}) holding values in the range $few \times 10^{20} - few \times 10^{23}$ atoms cm^{-2}. Therefore, according to Wilms et al. (2000), the observed spectrum can be related to the real spectrum of a source through the relation

$$S_{\text{obs}}(E) = e^{-\sigma(E)N_H} S_{\text{source}}(E). \tag{17}$$

The photoelectric absorption effect, therefore, causes the X-ray spectra to bend-over towards lower energies. This can be considered in spectral fitting using the absorption models available in spectral fitting packages.

2.4.4   Fluorescence lines

The occurrence of absorption in the vicinity of the NS can also result in the appearance of fluorescent emission lines in the X-ray spectra. These features are produced by irradiation of the cold matter distributed around the NS. Such information provides useful information about the material within the strong gravitational field of the compact object, for example, the interior regions of the accretion disk. Through

Figure 10. Kα and Kβ fluorescence radiations. When an electron from L-shell (a) or M-shell (b) fills a vacant space in the most inner shell (K).
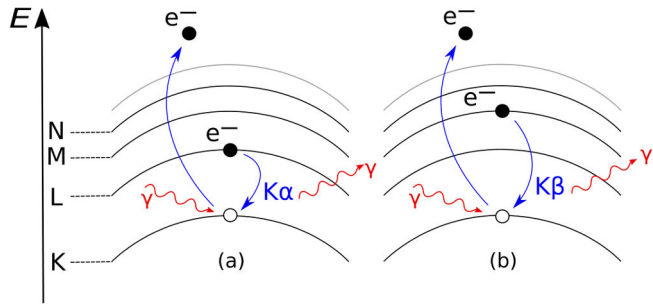
photoelectric absorption, the inner shell electron of an atom is excited to higher levels. Once the atom gets ionized, an electron from the outer shells fills the vacancy emitting photons with energies equal to the energy difference between the shells, e.g. iron Kα and Kβ fluorescence emissions in 6–7 keV (see Fig. 10).

The research presented in this dissertation only deals with fluorescence emission lines which can be empirically modeled by a simple Gaussian line profile discussed in sec. 3.2.2. Therefore, other atomic processes such as radiative recombination, radiative cascade, etc., are not discussed here.

2.4.5 Soft excess

If the soft X-rays emerged from XRPs are not heavily absorbed by Galactic gas, they may be characterized by a low-energy radiation component, the so-called soft excess, in the X-ray spectra (Hickox et al. 2004). This soft emission can mostly be modeled with a blackbody component (see Sec. 3.2.2) with temperatures $kT_{\rm BB} \sim 0.1$ keV. Although the origin of such a feature is still under debate, Hickox et al. (2004) concluded that the production mechanism depends strongly on the luminosity of the source. For low-luminosity pulsars, the low optical depth of the accretion column allows the soft X-rays to be emitted directly from the polar caps (La Palombara & Mereghetti 2006). Alternatively, the soft photons can be reprocessed by an optically thin photoionized or collisionally heated diffuse gas around the NS (Hickox et al. 2004). In high-luminosity sources, however, reprocessing of hard X-rays by the inner disk accretion material can be the dominant process to produce the soft excess (Hickox et al. 2004).

3 Observations and data analysis

3.1 X-ray observatories

X-rays are typically defined to have energies in the range ~0.1-100 keV over which the atmosphere of the Earth is opaque meaning no atmospheric transmission of electromagnetic radiation in this range is allowed. Thus, it is impossible to detect such high-energy radiations with ground-based detectors. The necessity of having X-ray detectors launched into space prevented X-ray astrophysics from emerging before the second half of the 20th century when the technological developments enabled us to perform space missions. In this section, the general characteristics of the cosmic X-ray observatories whose observations were analyzed in this thesis are briefly discussed. An overview of the key properties of the satellites can be found at the end of this section in Table 1.

3.1.1 *NuSTAR*

Nuclear Spectroscopic Telescope Array (*NuSTAR*) was launched on June 13, 2012 to be the first focusing hard X-ray telescope operating in a wide energy range 3–79 keV (Harrison et al. 2013). It consists of two co-aligned grazing incidence X-ray telescopes focusing X-rays onto two Focal Plane Modules, FPMA and FPMB, mounted at a focal length of 10.14 m away (see Fig. 11-right). The FPMs are composed of 2×2 independent set of CdZnTe detector units each with 32×32 pixels corresponding to a Field of View (FOV) of 12′. The readout procedure in the *NuSTAR* detectors is performed independently for each pixel by its own discriminator. This would prevent pile-up effect to happen up to a flux of 10^5 counts s^{-1} pixel^{-1}. The instruments have an angular resolution of 18″ Full Width at Half Maximum (FWHM) and spectral resolution of 0.4 and 10 keV (FWHM), respectively at 10 and 68 keV. These characteristics together with the wide energy coverage, make *NuSTAR* suitable to search and study the Cyclotron Resonant Scattering Features in the spectra of XRPs.

3.1.2 *XMM-Newton*

Operated by the European Space Agency (ESA), the X-ray Multi-mirror Mission (*XMM-Newton*; Jansen et al. 2001) was launched in December 10, 1999 carrying three co-aligned X-ray telescopes each equipped with a European Photon Imaging
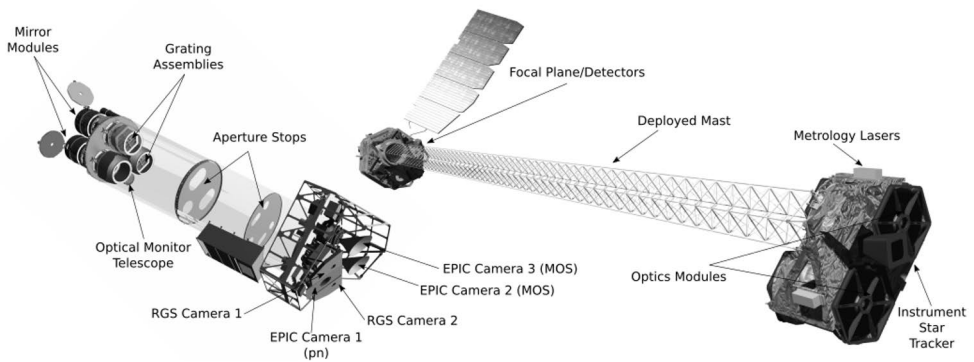
Figure 11. Schematics for the *XMM-Newton* observatory (*left*; adapted from `https://xmm-tools.cosmos.esa.int/external/xmm_user_support/documentation/uhb/overview.html`) and *NuSTAR* observatory (*right*; adopted from Harrison et al. 2013), and their instruments onboard.

Camera (EPIC) at the focus (Jansen et al. 2001). The EPIC consists of three medium spectral resolution detectors that are sensitive in the range 0.2–10 keV. The first camera, EPIC-pn, contains a 2×6 array of 200×64 pixel charge-coupled devices (CCDs) providing a large effective area of 1200 cm^2 at 1.3 keV (Strüder et al. 2001). Two other EPIC detectors are identical containing Metal Oxide Semiconductor (EPIC-MOS1 and EPIC-MOS2) CCD arrays (Turner et al. 2001). Each array consists of seven 600×600 pixel CCDs providing an effective area of 500 cm^2 at 1.3 keV. There are also two Reflection Grating Spectrometers (RGS) onboard *XMM-Newton* that enable high-resolution spectroscopy in the range 0.4–2.5 keV by collecting about half of the incident light passing through the MOS telescopes (Den Herder et al. 2001). The observatory also contains a 0.3 m optical/UV imaging telescope, the Optical Monitor (OM), which enables *XMM-Newton* to provide simultaneous X-ray and optical/UV observations (Mason et al. 2001). Fig. 11-left gives a schematic view of the observatory and its instruments. Data from RGS and OM instruments are not used in this thesis.

3.1.3 *Swift*

The Neil Gehrels *Swift* Observatory (Gehrels et al. 2004) was launched to low-Earth orbit on November 20, 2004, primarily dedicated to detecting Gamma-Ray Bursts (GRBs) and observing their afterglow in a broad energy range from optical to gamma-rays. To cope with this goal, the multi-wavelength observatory carries three instruments, Burst Alert Telescope (BAT; Barthelmy et al. 2005), X-Ray Telescope (XRT; Burrows et al. 2005), and Ultraviolet-Optical Telescope (UVOT; Roming et al. 2004) onboard (Fig. 13-left). The *Swift*/BAT telescope is designed to detect and lo-
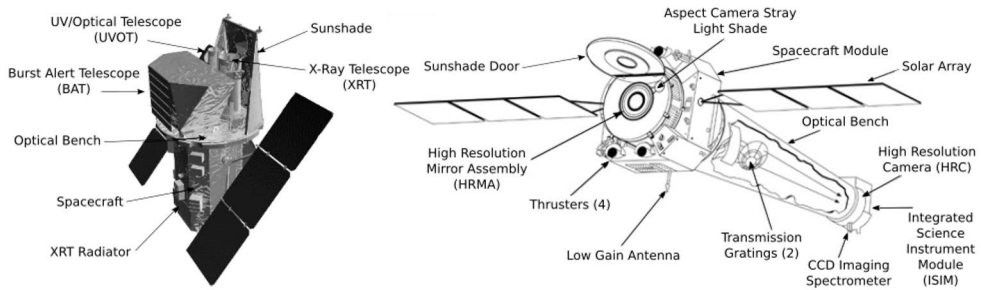
Figure 12. Schematics for the *Swift* observatory (*left*; adapted from `https://www.swift.ac.uk/about/instruments.php` and *Chandra* X-ray observatory (*right*; adapted from `https://chandra.harvard.edu/resources/illustrations/craftIllustrations.html`), and their onboard instruments.

calize a Gamma-Ray Burst (GRB; for a review see Sec. 3.3 of Atwood et al. 2009), within a position accuracy of 1–4′, as its large FOV allows it to monitor a big fraction of the sky. The BAT consists of an array of CdZnTe detectors operating in a wide energy range of 15–250 keV. Once a GRB is detected, BAT sends its position to the spacecraft to slew and point the two narrow-FOV XRT and UVOT at the source.

With an onboard X-ray imaging spectrometer (*Swift*/XRT) sensitive in 0.2–10 keV, *Swift* has made a significant contribution in X-ray astronomy especially in studying XRPs. XRT is a grazing incident Wolter type I telescope (similar to *XMM-Newton*) focusing the incident X-rays into a single 600×602 pixel CCD detector placed in a 3.5 m focal length. It has an effective area of about 125 cm^2 at 1.5 keV. Depending on the source brightness, the instrument operates in two different readout modes: Photon-Counting (PC) and Window Timing (WT). In the PC mode the entire CCD is read out to produce 2-D images allowing to have maximum spectral and spatial information but limited time resolution of 2.5 s. In the WT mode the CCD data is compressed into 1-D image to achieve high timing resolution of ~1.8 ms.

3.1.4 *Chandra*

Chandra X-ray observatory is the NASA's flagship X-ray mission launched on July 23, 1999 (Weisskopf et al. 2000). The high-resolution telescope was designed to perform deep-sky surveys and detailed study of hot plasmas through the universe. Similar to *XMM-Newton*, it is composed of a Wolter type-I grazing incidence telescope, the High Resolution Mirror Assembly (HRMA; Schwartz et al. 2000), that provides a spectacular angular resolution of 0.5″and an effective area of 800 cm^2 at 0.25 keV. The incident X-rays are focused into two different instruments mounted at a focal length of 10.06 m: the Advanced CCD Imaging Spectrometer (ACIS; Garmire et al.
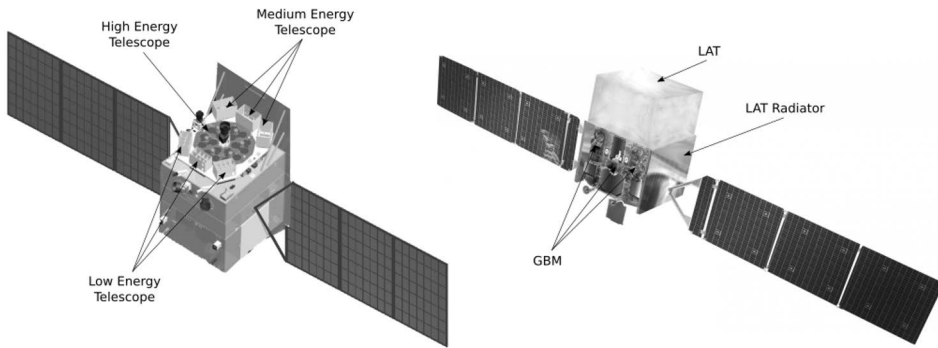
Figure 13. Schematics for the *Insight-HXMT* observatory (*left*; adapted from `https://spaceflight101.com/spacecraft/hxmt/`) and *Fermi* space observatory (*right*; adapted from `http://fermi.sonoma.edu/multimedia/gallery/index.php`), and their on-board instruments.

2003) and High Resolution Camera (HRC; Murray et al. 2000). In addition, there are also two high resolution spectrometers onboard, the High Energy Transmission Gratinga (HETG; Murray et al. 2000) and the Low Energy Transmission Grating (LETG; Brinkman et al. 1997) (see Fig. 12-right). Except for ACIS, observations obtained by other detectors were not used in this thesis, therefore, they will not be discussed further.

The ACIS consists of ten 1024×1024 pixel chips sorted in two different CCD arrays operating in the range of 0.3–10 keV. A 2×2 CCD array (ACIS-I) is optimized mainly for imaging. The rest of CCDs are lined-up in a 6×1 array (ACIS-S) for spectroscopy. ACIS-S can also be used with HETG for high-resolution spectroscopy. Two (out of 10) of the CCDs (labeled as S1 and S3) are back-illuminated providing a better spectral resolution (~95 eV at 1.5 keV) than the other eight chips in ACIS-S and ACIS-I which are front-illuminated chips. The latter provides an effective area of 600 cm^2 at 1.5 keV. Similar to *Swift*, *Chandra*/ASIC has two modes to readout the CCDs: Timed Exposure (TE) mode, providing a full-frame exposure with a frame time of 3.2 s, and Continuous Clocking (CC) mode, providing 1-D image (1×1024) with an exposure time of 2.85 ms.

3.1.5 *Insight-HXMT*

China's first X-ray satellite Hard X-ray Modulation Telescope (*HXMT*; also known as *Insight-HXMT*) was launched into low-Earth orbit (550 km altitude) on 15 June, 2017. It can provide observations in a wide energy range of 1–250 keV with a large effective area at high energies (Li 2007; Zhang et al. 2020). *Insight-HXMT* carries three X-ray instruments onboard (see Fig. 13-left), Low-Energy X-ray Telescope

(LE), Medium-Energy X-ray telescope (ME) and High-Energy X-ray telescope (HE). HE consists of 18 cylindrical NaI(Tl)/CsI(Na) crystal detectors together with a collimator providing a large effective area of ~5100 cm^2. The detectors operate in hard X-ray band 20–250 keV with a FOV of 1.1°×5.7°(FWHM). ME is consistent of 1728 Si-PIN detectors with a total effective area of 952 cm^2. It has a main FOV of 1°×4°covering the energy range of 5–30 keV. LE is equipped with 24 Swept Charge Devices (SCDs) which allow it to perform observations with high energy resolution of 140 eV at 5.9 keV in the range 1–15 keV. The readout procedure in SCDs detectors is carrying out in a fast and continuous mode providing an excellent time resolution of 1 ms as well as an extremely low pile-up which enable LE to observe very bright sources. The instrument has an effective area of 384 cm^2 and a main FOV of 1.6°×6°.

3.1.6 *Fermi*

The *Fermi* Gamma-ray Space Telescope was launched by NASA in 11 June 2008. It carries two main instruments, Gamma-ray Burst Monitor (GBM; von Kienlin et al. 2004; Meegan et al. 2009) and Large Area Telescope (LAT; Atwood et al. 2009) onboard (see Fig. 13-right). As it comes from its name, *Fermi* was originally designed to monitor the sky in gamma-rays exploring the most extreme environments from solar flares to gamma-ray bursts and jets in black holes. Although the GBM is mainly intended to detect gamma-ray bursts, it is also sensitive to hard X-rays above ~8 keV. GBM consists of 12 thin NaI scintillators (sensitive up to ~10 MeV) and 2 BGO detectors (sensitive in the energy range 150 keV to 30 MeV) mounted around the satellite. This design pattern allows GBM to provide a large FOV but not to resolve point sources. Thanks to the GBM Accreting Pulsars Program (GAPP; Malacaria et al. 2020), the GBM light curves and pulse measurements are available online[1] hence performing data reduction is not necessary. As no LAT observations were used in the current study, the instrument is not described here (see Atwood et al. (2009) for a full description).

---

[1] http://gammaray.nsstc.nasa.gov/gbm/science/pulsars/

Table 1. Overview of the key properties of the X-ray instruments used in this thesis.

Satellite/ Instrument	FOV (arcmin)	E-range[a] (keV)	$A(E)@E$[b] (cm^2) (keV)	ΔE @E[c] (keV) (keV)	Time-res.[d] (ms)
NuSTAR					
FPMA	12	3–79	850 @10	0.4 @10	0.002
FPMB	12	3–79	850 @10	0.4 @10	0.002
XMM-Newton					
EPIC-pn	30	0.15–15	1200 @1.3	0.15 @5.9	0.007–199.2
EPIC-MOS	30	0.2–10	500 @1.3	0.15 @5.9	1.75—2600
Swift					
XRT	23.5	0.2–10	125 @1.5	0.14 @5.9	1.8–2500
BAT	1500×900	15–250	1700 @60	7 @122	200
Chandra					
ACIS	16	0.3–10	500 @2	0.1 @3	2.85–3200
Insight-HXMT					
LE	96×360	1–15	384	0.15 @6	1
ME	60×240	5–30	952	3 @20	0.24
HE	66×342	20–250	5100	10.2 @60	0.004
Fermi					
GBM	all sky[e]	8–25000	126	15 @100	64

Notes: [a] Energy range of the instruments sensitivity. [b] Effective area at a certain energy. [c] Energy resolution at a certain energy. [d] Temporal resolution. [e] All sky not occulted by the Earth

3.2   X-ray data analysis

X-ray detectors collect observations in the so-called event list where the measurements of X-ray photons such as the arrival time and energy are recorded. Prior to analysis, each telescope's data reduction software packages should be used to extract the source light curves and energy spectra from the event files. As a next step, various timing and spectral methods can be used to analyze the resulting X-ray products described in the following subsections.

3.2.1   Timing analysis

Similar to other X-ray sources, accreting XRPs are also variable on timescales from milliseconds to years. These variabilities can be studied through the source light curves which are, in principle, the X-ray flux evolution of the source recorded as counts over time, i.e. time series. Timing analysis of the corresponding light curves can provide clues to the physical parameters of the binary system and the NS. These parameters include spin and orbital periods, the structure of emitting and occulting regions, and the magnetic field strength of the NS.

One of the most prominent and widely-used software to extract this information is HEASOFT which contains several packages. The HEASARC's general timing analysis package, XRONOS[2], contains several tasks such as *efsearch* and *efold*, providing strong tools to manipulate time series. *efsearch* task uses epoch folding technique (Davies 1990; Larsson 1996) to search for periodicity. In this method, for an arbitrary spin period in a predefined range, the χ^2 test is performed on the folded light curves, and the distribution of χ^2 values is plotted as a function of period. For a correct period, a large value of χ^2 appears at the pulsation period. Using the obtained periodicity, the pulse profile of the source of interest can be acquired at a given epoch using the task *efold*. Pulse profiles of an X-ray emitting pulsar can provide crucial information about the emission geometry (Nagase 1989) and beam pattern (see sec. 2.3.2).

3.2.2   Spectral analysis

X-ray spectroscopy is a useful tool to investigate the physical conditions in high-temperature plasma present in X-ray sources. However, the spectrometers' outputs are only the total photon counts (C) in a certain number of instrument energy channels (I) representing no actual spectrum of the source. Hence, one should consider the following expression to relate the observed spectrum to the intrinsic spectrum of

---

[2]https://heasarc.gsfc.nasa.gov/docs/software/heasoft/xanadu/xronos/manual/
xronos.html

the source:

$$C(I) = T \int_0^\infty R(I,E)A(E)S(E)dE, \tag{18}$$

where T is the total exposure time of observation in seconds, $R(I,E)$ is the unitless redistribution function of the instrument representing the probability of an incoming photon of energy E being detected in channel I, $A(E)$ denotes an energy-dependent function that accounts for the effective area of the instrument (cm^2) and $S(E)$ defines the source flux with the unit of photon cm^2 s^{-1} keV^{-1}. For each mission the functions $R(I,E)$ and $A(E)$ are given in the so-called Redistribution Matrix File (RMF) and Ancillary Response File (ARF), respectively. Inverting equation (18) to obtain the actual source spectrum is not possible since the redistribution matrices are usually not diagonal causing the solution tends to be unstable to statistical and systematic uncertainties in $C(I)$. Alternatively, a method of spectral fitting so-called *forward-folding* is used. In this approach, a proper theoretical model spectrum, which can best describe the physics of the source, is chosen and convolved with the detector response files (RMF and ARF). The initial model parameters are then iteratively modified in a given range until the so-called *best-fit values* of the parameters emerge. In this case, the difference between the observed and predicted data becomes minimized.

In order to evaluate whether a given model provides the most adequate description of the data, i.e the procedure is also known as the *goodness-of-fit*, different statistical methods can be utilized. When the data follow a Gaussian distribution, χ^2-statistic (see chapter 7 in Arnaud et al. 2011) is commonly used. Once the predicted count spectrum $C_P(I)$ is obtained for each energy channel, χ^2-statistic is defined as

$$\chi^2 = \sum \frac{(C(I) - C_P(I))^2}{\sigma^2(I)}, \tag{19}$$

where $\sigma(I)$ is the uncertainty for channel I. If the χ^2 value is close enough to the number of degrees of freedom (the total number of data points minus model parameters), the best fit is found. If the data contain a lower count rate following a Poisson distribution, the χ^2-statistic is not applicable. In this case, one should apply the so-called Cash-statistic which is a maximum likelihood-based statistic for Poisson data (Cash 1979).

Finding the best fit without knowing how well the parameters are constrained is not scientifically useful. Hence, the confidence interval for each parameter should be evaluated. In this case, the value of the parameter of interest v is varying until the $\Delta\chi^2 = \chi^2(v) - \chi^2_{best-fit}$ reach a particular amount depending on the confidence level required. For instance, for 68% (1σ) confidence level the $\Delta\chi^2 = 1$. Solving the equation for the value v results in two solutions which are considered the lower and upper limits of the selected parameter. Although the best-fit model is considered to well describe the source spectrum, there is no possibility showing the given model is physically correct. From the statistical point of view, several different models can

provide acceptable fits for the same observation, and choosing the correct model is a matter of scientific judgment.

Fortunately, there are some software packages that automatically do the above-mentioned routines. One of these programs is the X-ray spectral fitting package XSPEC (Arnaud 1996) which is a part of HEASOFT. XSPEC is a detector-independent software that makes it suitable to deal with data obtained by any X-ray satellites. Accordingly, all the spectral analyses in this work were performed using XSPEC which includes a wide range of spectral models and uses non-linear fitting methods to reach the best-fit parameters for the given model. Some of these spectral models are described in the following subsection.

Phenomenological Models

As already discussed in sec 2.4.1, several physical mechanisms are involved in producing X-ray emissions in accretion-powered XRPs. Therefore, it is extremely challenging to come up with a single model that describes all these processes at once. In addition to the theoretical model proposed by Becker & Wolff (2007) for bright XRPs, there are a few theoretical continuum models currently under development which are sensitive to low-luminous sources (Sokolova-Lapa et al. 2021; Mushtukov et al. 2021). Although these models show some success, no self-consistent physical models for continuum emission have been fully established yet in a broad range of mass accretion rates. In light of this, the phenomenological models should still be used, which are oversimplified and mostly consist of individual components. Nevertheless, they still may improve our understanding of the emitting source and, particularly in our case, the physics of accretion into XRPs. These models are available in two basic types: additive and multiplicative. The former type is an emission component modifying only a part of the spectrum such as a thermal emission (e.g. blackbody) or an emission line. Multiplicative models, on the other hand, modify the whole spectrum such as a cyclotron absorption line or a photoelectric absorption accounting for ISM. Following is a brief overview of the empirical models commonly used in this thesis.

As already discussed in sec. 2.4.1 the bulk and thermal Comptonization of seed X-ray photons results in a power-law-like shape of X-ray continuum characterized by a high-energy exponential cut-off at energies ~7–30 keV (see e.g. Filippova et al. 2005). A simple power-law model is described by

$$\texttt{powerlaw}(E) = KE^{-\alpha}, \tag{20}$$

where K is the normalization factor corresponding to the flux at 1 keV, E is the photon energy and α is the photon index which is expected to be in the range $0 < \alpha \leq 2$. Hence, the cut-off power-law functions are commonly used as phenomenological

models for XRPs spectral fitting such as:

cutoffpl. `cutoffpl` with just three free parameters is the most simple version of such models formulated as

$$\texttt{cutoffpl} = \texttt{powerlaw}(E) \times \exp(-E/E_{\text{fold}}), \tag{21}$$

where E_{fold} (E_{cut} in XSPEC) is the exponential folding energy.

highecut. The more flexible form of high-energy cut-off function is `highecut` (White et al. 1983) which has an additional free parameter, cut-off energy E_{cut}, but still quite quick to calculate. This model is commonly used together with a power law in the form of `powerlaw×highecut`:

$$M(E) = \texttt{powerlaw}(E) \times \begin{cases} \exp[(E_{\text{cut}} - E)/E_{\text{fold}}], & (E \geq E_{\text{cut}}) \\ 1, & (E \leq E_{\text{cut}}). \end{cases} \tag{22}$$

Since the exponential cut-off is mainly due to the thermal Comptonization, the folding energy in this model is mostly interpreted as electron temperature, kT_{e}, with a unit of keV. Unlike the `cutoffpl` model that steepens the continuum continuously, the multiplicative `highecut` model has a discontinuity in its first derivative at E_{cut}.

fdcut. The other form of this class of functions is a power-law with a Fermi-Dirac form of cut-off, the so-called `fdcut` model, which was defined by (Tanaka 1986) as

$$M(E) = \texttt{powerlaw}(E) \frac{1}{\exp((E - E_{\text{cut}})/E_{\text{fold}}) + 1}. \tag{23}$$

Similar to the previous model, `fdcut` also has four free parameters, however, the model should be manually introduced to XSPEC as it is not included in the package.

NPEX. Developed by (Mihara 1995), the Negative Positive power-law EXponential model (`NPEX`) is composed of the summation of two power-laws multiplied by an exponential roll-off:

$$\texttt{NPEX}(E) = (K_1 E^{-\alpha_1} + K_2 E^{+\alpha_2}) \exp(-E/kT). \tag{24}$$

As suggested by its name, the photon indices in the model are of opposite signs (negative and positive) where the second one, α_2, is set to a value of two. The `NPEX` model, in this context, is essentially a combination of `cutoffpl` and a Wien hump. Therefore, `NPEX` is a useful model to fit both soft and hard parts of the X-ray spectra of some XRPs.

For modeling the other spectral components such as emission lines and absorption features the following models are widely used:

gauss. The Gaussian line profile, `gauss` model, can be used for different purposes, e.g. modeling the soft excess in X-ray spectra. However, it is commonly used to model emission lines such as iron fluorescence emissions. `gauss` is calculated by

$$\texttt{gauss}(E) = \frac{K}{\sigma \sqrt{2\pi}} \exp\left(-\frac{(E - E_{\text{line}})^2}{2\sigma^2}\right). \tag{25}$$

Here, E_{line} and σ are the line energy and width in keV and K is the total flux within the line photons s^{-1} cm^{-2}.

GABS. For most of XRPs a Gaussian absorption profile can be used to fit the possible CRSFs in their X-ray spectra. The multiplicative Gaussian absorption line model, GABS, is defined as

$$\texttt{GABS}(E) = \exp\left[-\left(\frac{\tau_{\text{line}}}{\sqrt{2\pi}\sigma_{\text{line}}}\right) \exp\left(-\frac{(E - E_{\text{line}})^2}{2\sigma_{\text{line}}^2}\right)\right], \tag{26}$$

where E_{line} is the line centroid energy and σ_{line} and τ_{line} characterize the line width and depth, respectively. The optical depth at the line center can be calculated as $\tau_{\text{line}}/(\sigma_{\text{line}} \sqrt{2\pi})$. It should be noted that the Gaussian profile represents a Maxwellian distribution of atoms occurring as a result of their thermal motion and such an approach is completely different from the physics of CRSFs. Thus, the GABS model is not physically justified for CRSFs.

3.3 Optical Surveys

Two of the XRPs investigated in this thesis, Swift J1816.7−1613 and 2S 1845−024, were poorly studied X-ray sources in which the nature of the optical companion as well as the distance to the source were unknown. According to the methods already tested and explained by Karasev et al. (2010, 2015), if the magnitudes of the subjected star are known in at least two near-infrared (IR) filters, i.e. H and K, it would be possible to obtain the distance and absorption along with the Galactic bulge which the source is located at. By evaluating the absorption magnitude along the line of sight to the source, the possible distance and the spectral class of the companion star can be roughly determined. For this, the latest data of the public release of the UKIRT Infrared Deep Sky Galactic Plane Survey (UKIDSS-GPS)[3] and *Spitzer*/GLIMPSE[4] surveys were used.

UKIDSS-GPS is one of the five public surveys based on the United Kingdom Infrared Telescope (UKIRT) which uses a Wide Field Camera (WFCAM; Casali et al. 2007). UKIDSS-GPS is a near-IR survey operating in three J, H, and K bands (1-3

---

[3]http://surveys.roe.ac.uk/wsa/

[4]http://vizier.u-strasbg.fr/viz-bin/VizieR?-source=%20GLIMPSE

μm; Lucas et al. 2008) which maps over 1800 deg^2 of northern and equatorial parts of the Galactic plane. Galactic Legacy Infrared Midplane Survey Extraordinaire (GLIMPSE; Benjamin et al. 2003) is also a IR survey which was using the Infrared Array Camera (IRAC; Fazio et al. 1998) onboard *Spitzer* (Gallagher et al. 2003) at 3.6, 4.5, 5.8, and 8.0 μm. *Spitzer* IR space telescope which was launched and operated by NASA since 2003, ended its mission on 30 January 2020. GLIMPSE was aimed to map IR emission from the inner Galactic disk.

4 Summary of the original publications

4.1 Properties of the transient X-ray pulsar Swift J1816.7–1613 and its optical companion

In this paper, we report on the results of the X-ray and IR analysis of the poorly studied X-ray pulsar Swift J1816.7−1613 on its way to quiescence from a type I outburst. For this, the data obtained from *Swift*, *NuSTAR* and *Chandra* observatories together with the IR data from UKIDSS/GPS and *Spitzer*/GLIMPSE surveys were used. Having aimed to determine the magnetic field strength of the source we searched for cyclotron absorption lines in the broad-band energy spectrum, however, no such lines were detected. Therefore, using timing analysis the magnetic field was estimated to be in the range of a few $\times 10^{11}$ to a few $\times 10^{12}$ G as it is typical for XRPs. In addition, the IR analysis determined the IR-companion as a B0-2e star which is located at a distance of 7–13 kpc.

4.2 *NuSTAR* Observations of the Wind-fed X-Ray Pulsar GX 301−2 During an Unusual Spin-up Event

In this paper, we describe the properties of the well-known wind-accreting X-ray pulsar GX 301−2 through the strong spin-up episode occurred in January-March 2019. For this, we used the single *NuSTAR* observation performed during this episode together with two other *NuSTAR* observations obtained earlier in 2014 and 2015 in order to compare the source parameters on and off the rare and strong spin-up episodes. As a result, we detected only minor differences in spectral and timing properties of the source during the spin-up, and the normal wind-fed state. This presumably can associated with the formation of a transient accretion disk, as expected, during such episodes. We then discussed the possible reasons for the lack of any significant variations in most of the observed source properties in light of the conditions for disk formation and concluded that the observed X-ray emission is due to simultaneous accretion directly from the wind and through a transient accretion disk during the spin-up episode.

4.3 Spectral evolution of X-ray pulsar 4U 1901+03 during 2019 outburst based on *Insight-HXMT* and *NuSTAR* observations

We present a detailed X-ray spectral analysis of X-ray pulsar 4U 1901+03 using the observations obtained by the *Insight-HXMT* and *NuSTAR* observatories during the source outburst in 2019. 4U 1901+03 had showed a controversial absorption feature at around 10 keV in previous *RXTE* observations of the source. Hence, with a focus on the properties of this putative absorption feature, we used the *Insight-HXMT* data with an extensive coverage of the outburst to study the spectral evolution of the source as a function of flux. As a result, the structure of the 10-keV feature is found to be highly dependent on the choice of continuum model. In particular, we showed that a two-component model can describe the broadband spectrum of the source with inclusion of no absorption component at 10 keV. We also performed a detail phase-averaged and phase-resolved spectral analyses with a focus on another absorption feature at around 30 keV recently reported in the *NuSTAR* data. The 30-keV feature was detected significantly in the both phase-averaged and phase-resolved spectra irrespective of the continuum model.

4.4 Broad-band analysis of X-ray pulsar 2S 1845−024

In this paper, we report on the timing and spectral properties of the poorly studied XRP 2S 1845−024 using *NuSTAR* observations performed during the type I outburst in 2017. We did not detect any cyclotron absorption feature in the phase-averaged and phase-resolved spectra of the source. We also used X-ray data obtained by *Swift*, *XMM-Newton* and *Chandra* satellites to investigate the spectral properties as a function of orbital phase which revealed a high hydrogen column density for 2S 1845−024 reaching the maximum value $\sim 10^{24}$ cm^{-2} during the periastron passage. The high-quality *Chandra* observation enabled us to localize the source accurately at R.A. = $18^h48^m16^s.8$ and Dec. = $-2°25'25''.1$ (J2000). This consequently allowed us to use infrared (IR) survey data in order to roughly determine the type of the optical counterpart in 2S 1845−024 to be an OB supergiant located at the distance $\gtrsim 15$ kpc.

4.5   The author's contribution to the publications

Paper I. Properties of the transient X-ray pulsar Swift J1816.7–1613 and its optical companion

The X-ray data reduction and the majority of the spectral and temporal analyses were carried out by the author of the thesis. The author also contributed to the main idea and prepared most of the manuscript.

Paper II. NuSTAR Observations of the Wind-fed X-Ray Pulsar GX 301–2 During an Unusual Spin-up Event

The author contributed to the main idea of the paper, reduced the X-ray observations and performed the majority of the data analyses. The author also prepared most of the manuscript.

Paper III. Spectral evolution of X-ray pulsar 4U 1901+03 during 2019 outburst based on Insight-HXMT and NuSTAR observations

The author independently performed all the X-ray data analysis and the statistical tests and produced all the figures and tables. In addition to contributing to the main idea of the paper, the author wrote the entire manuscript.

Paper IV. Broad-band analysis of X-ray pulsar 2S 1845–024

The author of the thesis compiled and analysed the X-ray data obtained by all four X-ray satellites and produced all the figures and tables of the X-ray part. The majority of the manuscript was written by the author.

5 Future research

It is of great interest to detect absorption features originating from accreting XRPs, since they allow us to measure the magnetic fields directly. However, the results presented in this thesis demonstrate that interpretation of a possible absorption feature in the spectrum of a particular X-ray pulsar is highly dependent on the choice of continuum model. For instance, in XRP 4U 1901+03, we suggested that a double-component continuum model can describe the X-ray spectrum with inclusion of no absorption component. The transformation of a typical cutoff power-law-shaped spectrum observed in high luminosity XRPs to a double-component spectrum mostly occurs at low luminosities. My results support this idea that such a double-component continuum can also be seen in high luminosity sources. Since the gap between the low- and high-energy components can be interpreted as an absorption feature, it is important to study the formation and evolution of the double-component continuum from both a statistical and physical points of view. The large field of view as well as the sky-survey mode of *eROSITA* provide a perfect chance of detecting low-luminous sources. This together with *NuSTAR* observations would enable us to collect large sample of sources to investigate the evolution of the double-component continuum both in their low and high states. The results of this study can be compared with physically motivated theoretical models which have recently appeared and demonstrate significant consistency with the observational data on low-luminosity XRPs (Mushtukov et al. 2021; Sokolova-Lapa et al. 2021).

List of References

Arnaud, K. A. 1996, in Astronomical Society of the Pacific Conference Series, Vol. 101, Astronomical Data Analysis Software and Systems V, ed. G. H. Jacoby & J. Barnes, 17

Arnaud, K. A., Smith, R. K., & Siemiginowaska, A. 2011, Handbook of X-ray Astronomy, Cambridge Observing Handbooks for Research Astronomers (Cambridge University Press)

Atwood, W. B., Abdo, A. A., Ackermann, M., et al. 2009, ApJ, 697, 1071

Baade, W. & Zwicky, F. 1934, Physical Review, 46, 76

Bachetti, M., Harrison, F. A., Walton, D. J., et al. 2014, Nature, 514, 202

Baron, E. & Cooperstein, J. 1990, ApJ, 353, 597

Barthelmy, S. D., Barbier, L. M., Cummings, J. R., et al. 2005, Space Sci. Rev., 120, 143

Basko, M. M. & Sunyaev, R. A. 1975, A&A, 42, 311

Basko, M. M. & Sunyaev, R. A. 1976, MNRAS, 175, 395

Becker, P. A. 1998, ApJ, 498, 790

Becker, P. A., Klochkov, D., Schönherr, G., et al. 2012, A&A, 544, A123

Becker, P. A. & Wolff, M. T. 2005a, ApJ, 621, L45

Becker, P. A. & Wolff, M. T. 2005b, ApJ, 630, 465

Becker, P. A. & Wolff, M. T. 2007, The Astrophysical Journal, 654, 435

Beloborodov, A. M. 2002, ApJ, 566, L85

Benjamin, R. A., Churchwell, E., Babler, B. L., et al. 2003, PASP, 115, 953

Bethe, H. A. 1990, Reviews of Modern Physics, 62, 801

Bethe, H. A., Brown, G. E., & Lee, C. H. 2003, Formation and evolution of black holes in the Galaxy : selected papers with commentary, Vol. 33

Bhattacharya, D. & van den Heuvel, E. 1991, Physics Reports, 203, 1

Blondin, J. M., Kallman, T. R., Fryxell, B. A., & Taam, R. E. 1990, ApJ, 356, 591

Brandt, N. & Podsiadlowski, P. 1995, MNRAS, 274, 461

Brice, N., Zane, S., Turolla, R., & Wu, K. 2021, MNRAS, 504, 701

Brinkman, A. C., Gunsing, C. J., Kaastra, J. S., et al. 1997, in Society of Photo-Optical Instrumentation Engineers (SPIE) Conference Series, Vol. 3113, Grazing Incidence and Multilayer X-Ray Optical Systems, ed. R. B. Hoover & A. B. Walker, 181–192

Burnard, D. J., Arons, J., & Klein, R. I. 1991, ApJ, 367, 575

Burnard, D. J., Klein, R. I., & Arons, J. 1988, ApJ, 324, 1001

Burrows, D. N., Hill, J. E., Nousek, J. A., et al. 2005, Space Sci. Rev., 120, 165

Bykov, A. M. & Krasil'shchikov, A. M. 2004, Astronomy Letters, 30, 309

Campana, S., Gastaldello, F., Stella, L., et al. 2001, ApJ, 561, 924

Canuto, V. & Ventura, J. 1977, Fund. Cosmic Phys., 2, 203

Casali, M., Adamson, A., Alves de Oliveira, C., et al. 2007, A&A, 467, 777

Cash, W. 1979, ApJ, 228, 939

Chadwick, J. 1932, Nature, 129, 312

Chen, X., Wang, W., Tang, Y. M., et al. 2021, ApJ, 919, 33

Coburn, W., Heindl, W. A., Gruber, D. E., et al. 2001, ApJ, 552, 738

Colbert, E. J. M., Heckman, T. M., Ptak, A. F., Strickland, D. K., & Weaver, K. A. 2004, ApJ, 602, 231

Corbet, R. H. D. 1986, MNRAS, 220, 1047

Davidson, K. & Ostriker, J. P. 1973, ApJ, 179, 585

Davies, S. R. 1990, MNRAS, 244, 93

Den Herder, J. W., Brinkman, A. C., Kahn, S. M., & et al. 2001, A&A, 365, L7

Di Salvo, T., Burderi, L., Robba, N. R., & Guainazzi, M. 1998, ApJ, 509, 897

El Mellah, I., Sander, A. A. C., Sundqvist, J. O., & Keppens, R. 2019, A&A, 622, A189

Fabbiano, G. 1989, ARA&A, 27, 87

Farinelli, R., Ceccobello, C., Romano, P., & Titarchuk, L. 2012, A&A, 538, A67

Farinelli, R., Ferrigno, C., Bozzo, E., & Becker, P. A. 2016, A&A, 591, A29

Fazio, G. G., Hora, J. L., Willner, S. P., et al. 1998, in Society of Photo-Optical Instrumentation Engineers (SPIE) Conference Series, Vol. 3354, Infrared Astronomical Instrumentation, ed. A. M. Fowler, 1024–1031

Ferrigno, C., Becker, P. A., Segreto, A., Mineo, T., & Santangelo, A. 2009, A&A, 498, 825

Filippova, E. V., Tsygankov, S. S., Lutovinov, A. A., & Sunyaev, R. A. 2005, Astronomy Letters, 31, 729

Finger, M. H., Bildsten, L., Chakrabarty, D., et al. 1999, ApJ, 517, 449

Forman, W., Jones, C., Cominsky, L., et al. 1978, ApJS, 38, 357

Friedman, H., Lichtman, S. W., & Byram, E. T. 1951, Physical Review, 83, 1025

Fürst, F., Suchy, S., Kreykenbohm, I., et al. 2011, A&A, 535, A9

Gallagher, D. B., Irace, W. R., & Werner, M. W. 2003, in Society of Photo-Optical Instrumentation Engineers (SPIE) Conference Series, Vol. 4850, IR Space Telescopes and Instruments, ed. J. C. Mather, 17–29

Gandolfi, S., Carlson, J., & Reddy, S. 2012, Phys. Rev. C, 85, 032801

Garmire, G. P., Bautz, M. W., Ford, P. G., Nousek, J. A., & Ricker, George R., J. 2003, in Society of Photo-Optical Instrumentation Engineers (SPIE) Conference Series, Vol. 4851, X-Ray and Gamma-Ray Telescopes and Instruments for Astronomy., ed. J. E. Truemper & H. D. Tananbaum, 28–44

Gehrels, N., Chincarini, G., Giommi, P., et al. 2004, ApJ, 611, 1005

Ghosh, P. & Lamb, F. K. 1978, ApJ, 223, L83

Ghosh, P. & Lamb, F. K. 1979, ApJ, 232, 259

Giacconi, R., Gursky, H., Kellogg, E., Schreier, E., & Tananbaum, H. 1971, ApJ, 167, L67

Giacconi, R., Gursky, H., Paolini, F. R., & Rossi, B. B. 1962, Phys. Rev. Lett., 9, 439

Giacconi, R., Murray, S., Gursky, H., et al. 1972, ApJ, 178, 281

Grimm, H. J., Gilfanov, M., & Sunyaev, R. 2002, A&A, 391, 923

Harrison, F. A., Craig, W. W., Christensen, F. E., et al. 2013, ApJ, 770, 103

Hayakawa, S. & Matsuoka, M. 1964, Progress of Theoretical Physics Supplement, 30, 204

Heemskerk, M. H. M. & van Paradijs, J. 1989, A&A, 223, 154

Hickox, R. C., Narayan, R., & Kallman, T. R. 2004, ApJ, 614, 881

Hilditch, R. W. 2001, An Introduction to Close Binary Stars

Hutchings, J. B., Crampton, D., Cowley, A. P., & Osmer, P. S. 1977, ApJ, 217, 186

Illarionov, A. F. & Sunyaev, R. A. 1975, A&A, 39, 185

Israel, G. L., Belfiore, A., Stella, L., et al. 2017, Science, 355, 817

Jansen, F., Lumb, D., Altieri, B., & et al. 2001, A&A, 365, L1

Karasev, D. I., Lutovinov, A. A., & Burenin, R. A. 2010, MNRAS, 409, L69

Karasev, D. I., Tsygankov, S. S., & Lutovinov, A. A. 2015, Astronomy Letters, 41, 394

Karino, S., Nakamura, K., & Taani, A. 2019, PASJ, 71, 58

Klochkov, D., Doroshenko, V., Santangelo, A., et al. 2012, A&A, 542, L28

Koester, D. & Chanmugam, G. 1990, Reports on Progress in Physics, 53, 837

Kraus, U., Zahn, C., Weth, C., & Ruder, H. 2003, ApJ, 590, 424

Kretschmar, P. 1996, PhD thesis, Eberhard Karls University of Tubingen, Germany

Kretschmar, P., Fürst, F., Sidoli, L., et al. 2019, NewAR, 86, 101546

Kühnel, M., Müller, S., Kreykenbohm, I., et al. 2013, A&A, 555, A95

La Barbera, A., Burderi, L., Di Salvo, T., Iaria, R., & Robba, N. R. 2001, ApJ, 553, 375

La Palombara, N. & Mereghetti, S. 2006, A&A, 455, 283

Lai, D. 2001, Reviews of Modern Physics, 73, 629

Lai, D. 2014, in European Physical Journal Web of Conferences, Vol. 64, Physics at the Magnetospheric Boundary, 01001

Langer, S. H. & Rappaport, S. 1982, ApJ, 257, 733

Larsson, S. 1996, A&AS, 117, 197

Lasota, J.-P. 2001, NewAR, 45, 449

Lewin, W. H. G., van Paradijs, J., & van den Heuvel, E. P. J. 1997, X-ray Binaries (Cambridge, UK: Cambridge University Press)

Li, T.-P. 2007, Nuclear Physics B Proceedings Supplements, 166, 131

Liu, J., Jenke, P. A., Ji, L., et al. 2022, MNRAS, 512, 5686

Liu, Q. Z., van Paradijs, J., & van den Heuvel, E. P. J. 2006, A&A, 455, 1165

Liu, Q. Z., van Paradijs, J., & van den Heuvel, E. P. J. 2007, A&A, 469, 807

Long, K. S. & van Speybroeck, L. P. 1983, in Accretion-Driven Stellar X-ray Sources, ed. W. H. G. Lewin & E. P. J. van den Heuvel, 117–146

Lucas, P. W., Hoare, M. G., Longmore, A., et al. 2008, MNRAS, 391, 136

Lutovinov, A., Tsygankov, S., & Chernyakova, M. 2012, MNRAS, 423, 1978

Lutovinov, A. A., Tsygankov, S. S., Krivonos, R. A., Molkov, S. V., & Poutanen, J. 2017, ApJ, 834, 209

Lutovinov, A. A., Tsygankov, S. S., Suleimanov, V. F., et al. 2015, MNRAS, 448, 2175

Lynds, C. R. 1967, ApJ, 149, L41

Lyne, A. G., Manchester, R. N., & Taylor, J. H. 1985, MNRAS, 213, 613

Malacaria, C., Jenke, P., Roberts, O. J., et al. 2020, ApJ, 896, 90

Manchester, R. N., Hobbs, G. B., Teoh, A., & Hobbs, M. 2005, VizieR Online Data Catalog, VII/245

Martínez-Núñez, S., Kretschmar, P., Bozzo, E., et al. 2017, Space Sci. Rev., 212, 59

Martínez-Núñez, S., Torrejón, J. M., Kühnel, M., et al. 2014, A&A, 563, A70

Mason, K. O., Breeveld, A., Much, R., & et al. 2001, A&A, 365, L36

Meegan, C., Lichti, G., Bhat, P. N., et al. 2009, ApJ, 702, 791

Mészáros, P. 1984, in American Institute of Physics Conference Series, Vol. 115, High Energy Transients in AstroPhysics, ed. S. E. Woosley, 165–178

Meszaros, P., Harding, A. K., Kirk, J. G., & Galloway, D. J. 1983, ApJ, 266, L33

Meszaros, P. & Nagel, W. 1985, ApJ, 299, 138

Mihara, T. 1995, PhD thesis, -

Mihara, T., Makishima, K., & Nagase, F. 2004, ApJ, 610, 390

Miller, M. C. & Lamb, F. K. 2016, European Physical Journal A, 52, 63

Moritani, Y., Nogami, D., Okazaki, A. T., et al. 2013, PASJ, 65, 83

Murray, S. S., Austin, G. K., Chappell, J. H., et al. 2000, in Society of Photo-Optical Instrumentation Engineers (SPIE) Conference Series, Vol. 4012, X-Ray Optics, Instruments, and Missions III, ed. J. E. Truemper & B. Aschenbach, 68–80

Mushtukov, A. A., Suleimanov, V. F., Tsygankov, S. S., & Portegies Zwart, S. 2021, MNRAS, 503, 5193

Mushtukov, A. A., Suleimanov, V. F., Tsygankov, S. S., & Poutanen, J. 2015a, MNRAS, 454, 2539

Mushtukov, A. A., Suleimanov, V. F., Tsygankov, S. S., & Poutanen, J. 2015b, MNRAS, 447, 1847

Mushtukov, A. A., Verhagen, P. A., Tsygankov, S. S., et al. 2018, MNRAS, 474, 5425

Nabizadeh, A., Mönkkönen, J., Tsygankov, S. S., et al. 2019, A&A, 629, A101

Nabizadeh, A., Tsygankov, S. S., Molkov, S. V., et al. 2022, A&A, 657, A58

Nagase, F. 1989, PASJ, 41, 1

Nagel, W. 1981a, ApJ, 251, 288

Nagel, W. 1981b, ApJ, 251, 278

Nakajima, M., Mihara, T., Makishima, K., & Niko, H. 2006, ApJ, 646, 1125

Nelson, R. W., Wang, J. C. L., Salpeter, E. E., & Wasserman, I. 1995, ApJ, 438, L99

Okazaki, A. T., Hayasaki, K., & Moritani, Y. 2013, PASJ, 65, 41

Okazaki, A. T. & Negueruela, I. 2001, A&A, 377, 161

Porter, J. M. & Rivinius, T. 2003, PASP, 115, 1153

Postnov, K. A., Gornostaev, M. I., Klochkov, D., et al. 2015, MNRAS, 452, 1601

Poutanen, J. & Beloborodov, A. M. 2006, MNRAS, 373, 836

Poutanen, J., Mushtukov, A. A., Suleimanov, V. F., et al. 2013, ApJ, 777, 115

Prendergast, K. H. & Burbidge, G. R. 1968, ApJ, 151, L83

Reig, P. 2011, Ap&SS, 332, 1

Riffert, H. & Meszaros, P. 1988, ApJ, 325, 207

Rivinius, T., Carciofi, A. C., & Martayan, C. 2013, A&A Rev., 21, 69

Roming, P. W. A., Hunsberger, S. D., Mason, K. O., et al. 2004, in Society of Photo-Optical Instrumentation Engineers (SPIE) Conference Series, Vol. 5165, X-Ray and Gamma-Ray Instrumentation for Astronomy XIII, ed. K. A. Flanagan & O. H. W. Siegmund, 262–276

Rothschild, R. E., Kühnel, M., Pottschmidt, K., et al. 2017, MNRAS, 466, 2752

Sako, M., Kahn, S. M., Paerels, F., et al. 2003, arXiv e-prints, astroph/0309503

Schwartz, D. A., David, L. P., Donnelly, R. H., et al. 2000, in Society of Photo-Optical Instrumentation Engineers (SPIE) Conference Series, Vol. 4012, X-Ray Optics, Instruments, and Missions III, ed. J. E. Truemper & B. Aschenbach, 28–40

Sguera, V., Barlow, E. J., Bird, A. J., et al. 2005, A&A, 444, 221

Shklovsky, I. S. 1967, ApJ, 148, L1

Soker, N. 2004, MNRAS, 350, 1366

Sokolova-Lapa, E., Gornostaev, M., Wilms, J., et al. 2021, A&A, 651, A12

Staubert, R., Shakura, N. I., Postnov, K., et al. 2007, A&A, 465, L25

Staubert, R., Trümper, J., Kendziorra, E., et al. 2019, A&A, 622, A61

Strüder, L., Briel, U., Dennerl, K., & et al. 2001, A&A, 365, L18

Tanaka, Y. 1986, in Lecture Notes in Physics, Vol. 255, Radiation Hydrodynamics in Stars and Compact Objects, ed. D. Mihalas & K.-H. A. Winkler (Berlin: Springer-Verlag), 198

Tauris, T. M. & van den Heuvel, E. P. J. 2006, Formation and evolution of compact stellar X-ray sources, Vol. 39, 623–665

Tjemkes, S. A., Zuiderwijk, E. J., & van Paradijs, J. 1986, A&A, 154, 77

Townsend, L. J., Coe, M. J., Corbet, R. H. D., & Hill, A. B. 2011, MNRAS, 416, 1556

Truemper, J., Pietsch, W., Reppin, C., et al. 1978, ApJ, 219, L105

Tsygankov, S. S., Doroshenko, V., Lutovinov, A. A., Mushtukov, A. A., & Poutanen, J. 2017a, A&A, 605, A39

Tsygankov, S. S., Doroshenko, V., Mushtukov, A. A., et al. 2019a, MNRAS, 487, L30

Tsygankov, S. S., Lutovinov, A. A., Churazov, E. M., & Sunyaev, R. A. 2006, MNRAS, 371, 19

Tsygankov, S. S., Lutovinov, A. A., Churazov, E. M., & Sunyaev, R. A. 2007, Astronomy Letters, 33, 368

Tsygankov, S. S., Lutovinov, A. A., Doroshenko, V., et al. 2016, A&A, 593, A16

Tsygankov, S. S., Mushtukov, A. A., Suleimanov, V. F., et al. 2017b, A&A, 608, A17

Tsygankov, S. S., Rouco Escorial, A., Suleimanov, V. F., et al. 2019b, MNRAS, 483, L144

Turner, M. J. L., Abbey, A., Arnaud, M., & et al. 2001, A&A, 365, L27

Ustyugova, G. V., Koldoba, A. V., Romanova, M. M., & Lovelace, R. V. E. 2006, ApJ, 646, 304

Vasco, D., Klochkov, D., & Staubert, R. 2011, A&A, 532, A99

von Kienlin, A., Meegan, C. A., Lichti, G. G., et al. 2004, in Society of Photo-Optical Instrumentation Engineers (SPIE) Conference Series, Vol. 5488, UV and Gamma-Ray Space Telescope Systems, ed. G. Hasinger & M. J. L. Turner, 763–770

Walter, R., Lutovinov, A. A., Bozzo, E., & Tsygankov, S. S. 2015, A&A Rev., 23, 2

Weisskopf, M. C., Tananbaum, H. D., Van Speybroeck, L. P., & O'Dell, S. L. 2000, in Society of Photo-Optical Instrumentation Engineers (SPIE) Conference Series, Vol. 4012, X-Ray Optics, Instruments, and Missions III, ed. J. E. Truemper & B. Aschenbach, 2–16

Westphal, J. A., Sandage, A., & Kristian, J. 1968, ApJ, 154, 139

White, N. E., Swank, J. H., & Holt, S. S. 1983, ApJ, 270, 711

Wilms, J., Allen, A., & McCray, R. 2000, ApJ, 542, 914

Wolff, M. T., Becker, P. A., Gottlieb, A. M., et al. 2016, ApJ, 831, 194

Zeldovich, Y. B. & Guseynov, O. H. 1966, ApJ, 144, 840

Zhang, S.-N., Li, T., Lu, F., et al. 2020, Science China Physics, Mechanics, and Astronomy, 63, 249502